Petroleum Science 21 (2024) 1488–1507

Contents lists available at ScienceDirect

Petroleum Science

journal homepage: www.keaipublishing.com/en/journals/petroleum-science

Original Paper

Main controlling factor and mechanism of gas-in-place content of the Lower Cambrian shale from different sedimentary facies in the western Hubei area, South China

Gang Li [a], Xian-Ming Xiao [a, b, *], Bo-Wei Cheng [a], Chen-Gang Lu [a], Yue Feng [a], Dong-Sheng Li [a]

[a] School of Energy Resources, China University of Geosciences (Beijing), Beijing, 100083, China
[b] Frontiers Science Center for Deep-time Digital Earth, China University of Geosciences (Beijing), Beijing, 100083, China

ARTICLE INFO

Article history:
Received 14 May 2023
Received in revised form
16 September 2023
Accepted 13 December 2023
Available online 19 December 2023

Edited by Jie Hao and Meng-Jiao Zhou

Keywords:
Lower Cambrian shale
Deep-water shelf facies
Shallow-water platform facies
Pore structure
Methane adsorption
Gas-in-place content
Controlling factor

ABSTRACT

The Lower Cambrian shale gas in the western Hubei area, South China has a great resource prospect, but the gas-in-place (GIP) content in different sedimentary facies varies widely, and the relevant mechanism has been not well understood. In the present study, two sets of the Lower Cambrian shale samples from the Wells YD4 and YD5 in the western Hubei area, representing the deep-water shelf facies and shallow-water platform facies, respectively, were investigated on the differences of pore types, pore structure and methane adsorption capacity between them, and the main controlling factor and mechanism of their methane adsorption capacities and GIP contents were discussed. The results show that the organic matter (OM) pores in the YD4 shale samples are dominant, while the inorganic mineral (IM) pores in the YD5 shale samples are primary, with underdeveloped OM pores. The pore specific surface area (SSA) and pore volume (PV) of the YD4 shale samples are mainly from micropores and mesopores, respectively, while those of the YD5 shale samples are mainly from micropores and macropores, respectively. The methane adsorption capacity of the YD4 shale samples is significantly higher than that of the YD5 shale samples, with a maximum absolute adsorption capacity of 3.13 cm^3/g and 1.31 cm^3/g in average, respectively. Compared with the shallow-water platform shale, the deep-water shelf shale has a higher TOC content, a better kerogen type and more developed OM pores, which is the main mechanism for its higher adsorption capacity. The GIP content models based on two samples with a similar TOC content selected respectively from the Wells YD4 and YD5 further indicate that the GIP content of the deep-water shelf shale is mainly 3–4 m^3/t within a depth range of 1000–4000 m, with shale gas exploration and development potential, while the shallow-water platform shale has normally a GIP content of <1 m^3/t, with little shale gas potential. Considering the geological and geochemical conditions of shale gas formation and preservation, the deep-water shelf facies is the most favorable target for the Lower Cambrian shale gas exploration and development in the western Hubei area, South China.

1. Introduction

The Lower Cambrian shale in southern China formed in marine shelf and shallow-water platform environments under the background of Craton basin. The shale distributes extensively, generally with a thickness of 50–100 m and a TOC content of 2–10%, thus it is predicted to have huge shale gas resource potentials (Zou et al., 2010; Xiao et al., 2015; Liu et al., 2017; Cheng et al., 2018; Wei et al., 2018; Li et al., 2021). However, the shale has undergone several strong tectonic events such as Caledonian, Indosinian, Yanshanian and Himalayan (Zhang et al., 2019), and has been evolved to a very high maturity, with an equivalent vitrinite reflectance (EqR_o) value of 2.0–4.5% (Lin et al., 2014; Tian et al., 2015; Zhao et al., 2016; Luo et al., 2020; Wang, 2021; Meng et al., 2022), resulting in poor shale gas preservation conditions, especially outside the Sichuan Basin. The Lower Cambrian shale gas exploration has not achieved a substantial progress for a long

* Corresponding author.
E-mail address: xmxiao@cugb.edu.cn (X.-M. Xiao).

https://doi.org/10.1016/j.petsci.2023.12.012

period time (Lin et al., 2014; Ma et al., 2015; Ge et al., 2020; Wang, 2021; Li et al., 2022a).

Based on the available data of shale gas plays in the Sichuan Basin, Zhai et al. (2017a) proposed the shale gas accumulation model of "paleo-uplift margin" where shale gas reservoirs were believed to have a better formation and preservation condition than that of other areas. Following this model, more than 20 wells have been drilled with the target of the Lower Cambrian Shuijingtuo Formation strata, a shale-dominated strata with a relatively high TOC content, around the Huangling uplift in the western Hubei area in recent years, and some important findings have been obtained. For examples, the gas-in-place (GIP) content of the Lower Cambrian shale from the Well YD2 is 0.17–5.58 m^3/t, with an average of 2.24 m^3/t, and the shale interval with a GIP content of >2 m^3/t is 46 m thick; the Lower Cambrian shale from the Well ZD2 has also a GIP content of 0.23–4.45 m^3/t, and the average GIP content is as high as 2.88 m^3/t for the top quality 30 m interval (Luo et al., 2020; Xu et al., 2020). The major exploration breakthroughs of the Lower Cambrian shale gas in the western Hubei area have made this area become a new hotspot except for the Sichuan Basin for marine shale gas exploration in southern China.

However, according to the latest exploration results in the western Hubei area, the wells with a high GIP content of the Lower Cambrian shale are mainly located in the western and southern Huangling uplift, while for the wells in the east of the Huangling uplift, the Lower Cambrian shale has a poor GIP content, generally <0.5 m^3/t (Luo et al., 2020). Some studies suggested that the GIP content of the Lower Cambrian shale in the western Hubei area was mainly controlled by the maturity and/or preservation conditions restricted by structural deformation (Zhai et al., 2017a; Luo et al., 2019a, 2019b), but this explanation seems imperfect. Although the EqR_o value of the Lower Cambrian shale in the western Hubei area is relatively high, it is mostly between 2.0% and 3.0% (Luo et al., 2020), and generally <3.5%, the upper limit of EqR_o value for marine shales with commercial shale gas potentials proposed by Xiao et al. (2015). In addition, the eastern area of the Huangling uplift with a low GIP content has also a weak structural deformation, with good preservation conditions (Zhai et al., 2020).

According to the regional tectonic evolution and sedimentary background, the sedimentary facies were obviously variable in the western Hubei area during the Early Cambrian, including deep-water shelf facies, slope facies and shallow-water platform facies from southwest to northeast (Luo et al., 2020). The Lower Cambrian shales from different sedimentary facies are different not only in their thickness, but also in their geochemical characteristics (Chen et al., 2018; Shi, 2020). In recent years, there have been some related studies on the constraints of environmental conditions and sedimentary facies on the Lower Cambrian shale gas potential in the western Hubei area, and it has been gradually realized that the deep-water shelf facies is more favorable for the generation and storage of shale gas (Zhai et al., 2017b, 2019; Chen et al., 2018; Luo et al., 2020), which is quite similar to the Lower Silurian shale in southern China (Guo and Zhang, 2014; Pu et al., 2020). However, the mechanism of different GIP contents from different sedimentary facies shales is not clear, which also restricts the further exploration of the Lower Cambrian shale gas in the western Hubei area.

In the present study, the Lower Cambrian shale samples respectively from the deep-water shelf and shallow-water platform facies in the western Hubei area were studied. Through the field emission scanning electron microscope (FE-SEM) observation, low-pressure CO_2 adsorption (LPCA), low-pressure N_2 adsorption (LPNA) and high-pressure methane adsorption (HPMA) experiments, the differences of the two types of shales in their pore types, nanopore structure and methane adsorption capacity were investigated, and the effects of pore structure, TOC content, mineral composition, temperature and pressure on their methane adsorption capacity were discussed. Further, the GIP content models based on two typical samples from the two sedimentary facies were constructed, and the exploration and development potentials of shale gas were predicted.

2. Samples and experiments

2.1. Geological setting and samples

In the Late Sinian period, a subsidence occurred in the Yichang area of western Hubei, with the formation of several depressions with different scales, and then they were evolved into a tectonic paleogeographic pattern with uplifts and depressions in the Early Cambrian (Chen et al., 2018). Because of a massive transgression in the Yangtze Platform during this period, the sedimentary environment in the Yichang area varied from a deep-water shelf facies, a slope facies to a shallow-water platform facies from its southwest to northeast (Fig. 1(a)–(b)), which has directly affected the distribution of the Lower Cambrian Shuijingtuo Formation shale, with a decreasing thickness from southwest to northeast (Zuo et al., 2018; Luo et al., 2019a; Zhai et al., 2019).

In this study, a total of twenty shale samples of the Lower Cambrian Shuijingtuo Formation were selected from two wells (YD4 and YD5; ten samples for each well) in the Yichang area of western Hubei (Fig. 1(a)). The Wells YD4 and YD5 are located in the southern and northern Yichang slope belt, respectively, with the Lower Cambrian Shuijingtuo Formation shale of 155.28 m and 18.94 m in thickness (Fig. 1(c)), respectively, formed in the deep-water shelf and shallow-water platform environments, respectively (Zhang et al., 2019; Liu et al., 2022) (Fig. 1(a) and (b)). The shale samples were collected from the middle and bottom of the Shuijingtuo Formation, with current burial depth ranges of 1242.20–1328.75 m for the Well YD4 and 587.60–601.95 m for the Well YD5. It is worth noting that half of the YD4 shale samples were reported in their geochemistry by Li et al. (2023a), and these samples together with five newly-selected samples from the well form a TOC gradient which can be compared with the YD5 shale samples.

2.2. Methods and experiments

2.2.1. Geochemical analysis

The Lower Cambrian shale in southern China has been evolved to the high and over mature stages, and the reflectance of solid bitumen in the shale varies greatly (Wang et al., 2015). Therefore, in this study, the laser Raman spectral parameter of solid bitumen in the shale samples was used to determine their maturity. A HORIBA-JY Lab RAM automatic microscopic laser Raman spectrometer was used for this work with the main conditions as suggested by Zhou et al. (2014). The correlation equation between the laser Raman parameters and EqR_o is that EqR_o = 0.0537d (G − D) − 11.21 (Liu et al., 2013).

The LECO CS230 carbon/sulfur analyzer was used to determine the TOC content of the shale samples. Each sample (about 2 g) was grinded to 100 mesh, treated with dilute hydrochloric acid to remove the carbonate minerals, and then rinsed and dried. The treated samples were combusted with high temperature, and the TOC content was determined based on the CO_2 peak area.

The Rigaku MiniFlex-600 X-ray diffractometer was used to analyze the mineral compositions of the shale samples. The analysis conditions were described as Li et al. (2022b) and Feng et al. (2023a).

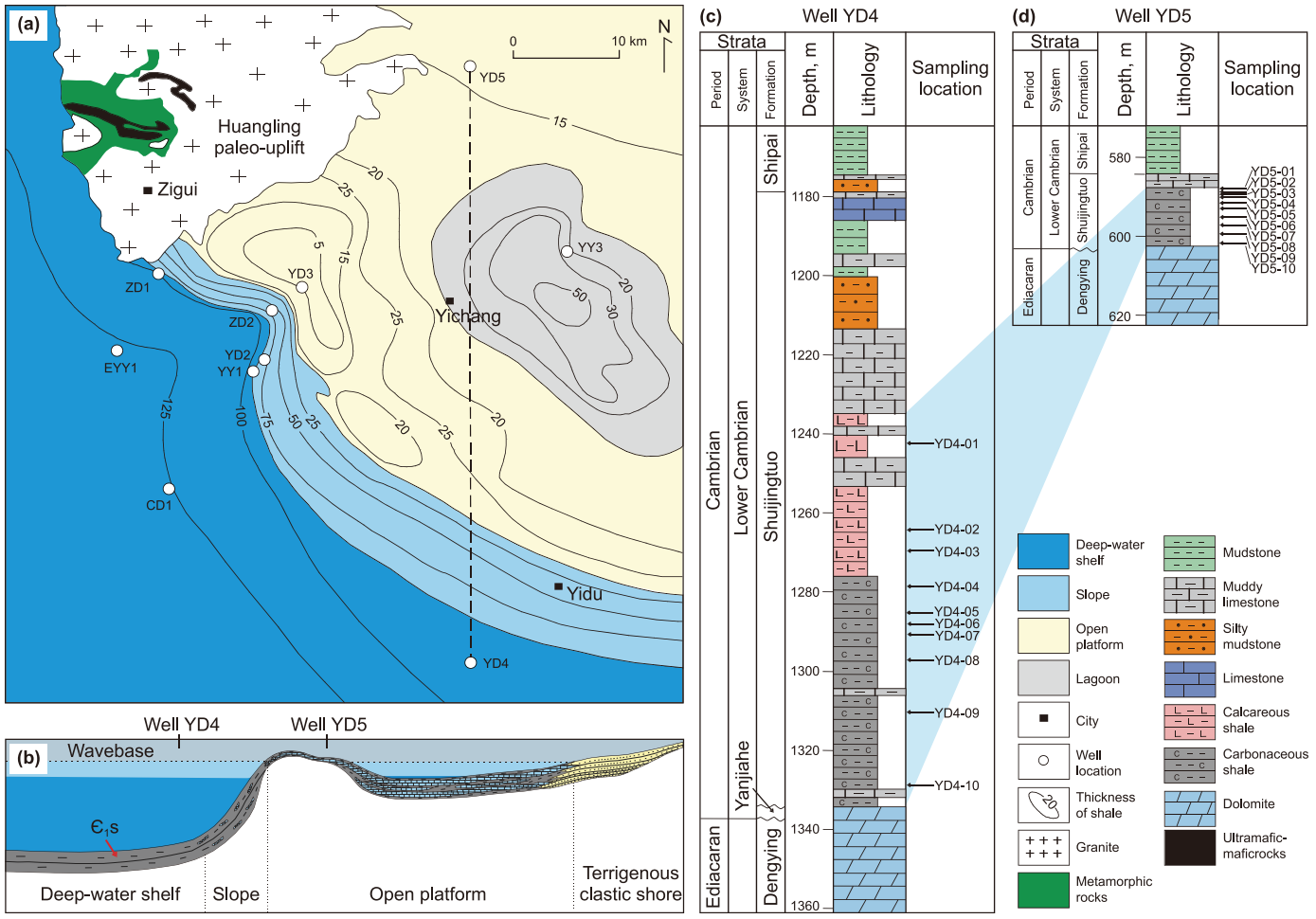

Fig. 1. Sedimentary characteristics of the Early Cambrian in the western Hubei area **(a)**, a south-north sedimentary section throughout this area **(b)**, and stratigraphic columns of the Lower Cambrian strata at the Well YD4 **(c)** and the Well YD5 **(d)**. (Modified from Zhai et al., 2019; Luo et al., 2020).

2.2.2. FE-SEM observation

The shale samples were polished firstly and then their pore characteristics were directly observed by the FE-SEM. The working conditions of the instrument were described by Tian et al. (2015).

2.2.3. Porosity measurement

The porosity of a shale sample was calculated using Eq. (1):

$$\phi = 1 - \frac{\rho_{sample}}{\rho_g} \tag{1}$$

where ϕ is porosity, %; ρ_{sample} and ρ_g are bulk density and grain density of the sample, respectively, cm^3/g.

2.2.4. Water saturation measurement

To calculate the shale GIP content, the water saturation of the YD4-01 and YD5-07 samples was measured using the drying method. The mass of the original samples was first weighed, and then dried under a near-vacuum condition (378.15 K, <30 mg Hg) to obtain the mass after the water was removed. The water content of the samples was calculated using Eq. (2):

$$C_w = \frac{1000\left(m - m_{dry}\right)}{m_{dry}} \tag{2}$$

where C_w is water content, mg/g; m and m_{dry} are the mass before and after drying, respectively, g.

The water saturation of the samples was determined using Eq. (3):

$$S_w = \frac{C_w \rho_{sample}}{10\phi\rho_w} \tag{3}$$

where S_w is water saturation, %; ρ_w is water density, i.e., 1 g/cm^3 as used by Sun et al. (2021).

2.2.5. LPCA and LPNA experiments

The instrument Micromeritics ASAP 2460 automatic surface area analyzer was used for the LPCA and LPNA experiments. The shale samples (1–2 g for each one) were pulverized and degassed under vacuum at 150 °C for 12 h, and then moved to the analyzer for the adsorption experiments.

The specific surface area (SSA), pore volume (PV) and size distribution of micropores and non-micropores were determined based on LPCA and LPNA data, respectively. The related equations were introduced by Li et al. (2022b). In this experiment, the non-micropores derived from the N_2 adsorption data include the mesopores (2–50 nm) and macropores (50–300 nm).

2.2.6. HPMA experiments

The instrument used for the HPMA experiment was a

Rubotherm Isosorp-Hpll Static high-pressure isothermal adsorption apparatus. About 5 g shale samples were loaded into the sample room, sealed and dried at 105 °C, and then the high purity helium was continuously injected for the buoyancy testing. After setting the equilibrium pressure point and equilibrium conditions, the high purity methane was injected, and the weight of the samples was recorded after equilibration at different pressure points. The adsorption capacity was calculated based on the volume and weight of the sample and methane density. For each sample, the setting temperature was 40 °C. For the samples YD4-01 and YD5-07, the HPMA experiments were carried out at three additional temperatures (25, 60 and 90 °C) to build their GIP geological models.

In this study, the supercritical Dubinin-Radushkevich (SDR) model and Gibbs adsorption theory were used to characterize the supercritical adsorption of methane in shales (Murata et al., 2001, 2002; Bae and Bhatia, 2006; Sakurovs et al., 2007; Rexer et al., 2013; Feng et al., 2023b). Under the experimental conditions, the excess and absolute adsorption capacities of methane were calculated as follows:

$$n_{\mathrm{exc}} = n_0 \exp\left\{ -D\left[\ln\left(\frac{\rho_{\mathrm{ad}}}{\rho_{\mathrm{f}}}\right)RT\right]^2\right\}\left(1 - \frac{\rho_{\mathrm{f}}}{\rho_{\mathrm{ad}}}\right) \tag{4}$$

$$n_{\mathrm{ab}} = \frac{n_{\mathrm{exc}}}{1 - \frac{\rho_{\mathrm{f}}}{\rho_{\mathrm{ad}}}} \tag{5}$$

where n_{exc}, n_0 and n_{ab} are excess adsorption capacity, maximum absolute adsorption capacity and absolute adsorption capacity, respectively, $\mathrm{cm^3/g}$; D is pore size distribution parameter, $\mathrm{mol^2/kJ^2}$; ρ_{ad} and ρ_{f} are adsorbed phase density and free phase density, respectively, $\mathrm{g/cm^3}$; R is a gas constant; T is experimental temperature, K.

Under geological conditions, the adsorbed, free and total gas contents were calculated using the following equations (Pan et al., 2016):

$$n^H_{\mathrm{exc}} = n^H_0 \exp\left\{ -D\left[\ln\left(\frac{\rho^H_{\mathrm{ad}}}{\rho^H_{\mathrm{f}}}\right)R(T_0 + HT_{\mathrm{g}})\right]^2\right\}\left(1 - \frac{\rho^H_{\mathrm{f}}}{\rho^H_{\mathrm{ad}}}\right) \tag{6}$$

$$n^H_{\mathrm{total}} = n^H_{\mathrm{exc}} + \frac{\phi(1 - S_{\mathrm{w}})}{\rho_{\mathrm{sample}}}\frac{\rho^H_{\mathrm{f}}}{\rho^{\mathrm{STP}}_{\mathrm{g}}} \tag{7}$$

$$n^H_{\mathrm{ab}} = \frac{n^H_{\mathrm{exc}}}{1 - \frac{\rho^H_{\mathrm{f}}}{\rho^H_{\mathrm{ad}}}} \tag{8}$$

$$n^H_{\mathrm{free}} = n^H_{\mathrm{total}} - n^H_{\mathrm{ab}} \tag{9}$$

where n^H_{exc}, n^H_0, n^H_{ab}, n^H_{total} and n^H_{free} are excess adsorption capacity, maximum absolute adsorption capacity, absolute adsorption capacity, total gas content and free gas content at a burial depth H, respectively, $\mathrm{cm^3/g}$; ρ^H_{ad} and ρ^H_{f} are adsorbed phase density and free phase density at a burial depth H, respectively, $\mathrm{g/cm^3}$; T_0 is surface temperature, K; T_{g} is geothermal gradient, K/100m; $\rho^{\mathrm{STP}}_{\mathrm{g}}$ is methane density at standard state (0 °C, 0.1 MPa), $\mathrm{g/cm^3}$.

3. Results

3.1. Geochemistry characteristics and mineral compositions

According to the experimental results, the TOC contents of the YD4 shale samples (representing deep-water shelf facies) and the YD5 shale samples (representing shallow-water platform facies) range from 0.43% to 10.70% (an average of 5.03%) and from 0.36% to 4.64% (an average of 1.95%), respectively. Overall, the TOC contents of shale samples from the two wells increase with the burial depth (Table 1), which is consistent with the Lower Cambrian shale in the northeastern Chongqing area reported by Meng et al. (2022).

Based on the laser Raman data, the EqR_o values of the four selected YD4 shale samples are 3.14–3.48%, with an average of 3.28%; the EqR_o values of the three selected YD5 shale samples are slightly lower, ranging from 2.80% to 2.99%, with an average of 2.83% (Table 1). Both sets of the shale samples are overmature, but do not exceed the upper limit of maturity (EqR_o = 3.5%) for a potential shale gas reservoir (Xiao et al., 2015).

The mineral compositions of the YD4 shale samples are mainly quartz, clay mineral and carbonate mineral, with contents of 20.4–65.8% (an average of 37.8%), 14.9–54.7% (an average of 25.4%) and 13.7–35.8% (an average of 22.7%), respectively. The contents of feldspar and pyrite are 3.8–18.6% (an average of 9.1%) and 1.9–14.8% (an average of 5.0%), respectively. Compared with the YD4 shale samples, the contents of quartz, carbonate mineral, feldspar and pyrite of the YD5 shale samples are less, with ranges of 20.7–45.3% (an average of 31.5%), 0–42.3% (an average of 11.0%), 0–5.2% (an average of 1.3%) and 0–4.0% (an average of 2.4%), respectively, while the clay mineral content is obviously higher, ranging from 21.2% to 71.6% (an average of 52.3%) (Table 1).

3.2. Pore types and porosity of shale samples

Based on the FE-SEM observation, the pores in the shale samples can be divided into three types: OM pores, inorganic mineral (IM) pores and microfractures, and the IM pores mainly include interparticle pores and intraparticle pores (Fig. 2).

The dominant pore type in the YD4 shale samples is OM pores although their IM pores also develop well (Fig. 2(a)–(e)). The shapes of OM pores are diverse, but most of them are spongy or oval, with a main pore size range of 10–40 nm (Fig. 2(a)). The OM pore face rate usually ranges from 10% to 30%, with an average of about 15%. Although the OM pores occur in pyrobitumen and kerogen, the former seems having more developed pores than the latter. The OM particles shielded by brittle minerals have well-preserved pores, especially the pyrobitumen among the pyrite framboids particles (Fig. 2(b)). The interparticle pores mostly belong to residual pores occurring between brittle minerals, and even between OM particles and minerals (Fig. 2(c)). The intraparticle pores are mainly present in carbonate minerals (Fig. 2(a), (e)) and clay minerals (Fig. 2(d)). In the former case, the pores are derived from the dissolution of carbonate minerals, mainly with round and oval shapes, while in the latter case, the pores are often filled with OM. The microfractures are mainly diagenetic microfractures (Fig. 2(e)), which are formed in diagenetic processes such as compaction or crystallization. They are mostly dendriform and have a greater length (more than a few microns), which can optimize the connectivity of pore systems.

The pores in the YD5 shale samples are mainly IM pores, and their OM pores are underdeveloped (Fig. 2(f)–(i)). The interparticle pores typically show an elongated shape, distributing between OM and brittle minerals or between two brittle minerals, generally with a pore size >50 nm (Fig. 2(f), (h)). Quite different from the YD4 shale samples, the YD5 shale samples develop relatively abundant

Table 1
The TOC content, EqR_o value, mineral composition and porosity of studied shale samples (The data of samples YD4-01, YD4-02, YD4-06, YD4-07 and YD4-08 are from Li et al. (2023a, b); nd: not detected).

Sample	Depth, m	Formation	TOC, %	EqR_o, %	Porosity, %	Mineral compositions, %							
						Quartz	K-feldspar	Plagioclase	Illite	Calcite	Dolomite	Pyrite	Others
YD4-01	1242.20	Shuijingtuo	2.45	3.26	4.86	21.6	0	8.5	54.7	9.1	2.6	3.4	0.1
YD4-02	1264.15	Shuijingtuo	3.13	3.23	4.14	39.7	0	9.8	31.8	11.9	4.2	2.6	0
YD4-03	1272.95	Shuijingtuo	3.85	nd	3.75	53.7	0	4.0	14.9	12.2	13.3	1.9	0
YD4-04	1278.70	Shuijingtuo	4.73	nd	4.32	65.8	0	3.8	16.8	5.8	5.0	2.8	0
YD4-05	1285.65	Shuijingtuo	6.03	3.48	4.22	33.9	0	4.4	18.2	18.6	10.1	14.8	0
YD4-06	1287.30	Shuijingtuo	8.21	nd	4.11	57.8	0	5.2	18.1	12.6	4.0	2.3	0
YD4-07	1290.75	Shuijingtuo	9.09	3.14	5.01	31.9	7.1	0	36.2	9.4	4.3	11.1	0
YD4-08	1296.35	Shuijingtuo	10.70	nd	4.95	20.4	18.6	0	22.6	16.5	15.4	6.5	0
YD4-09	1310.80	Shuijingtuo	0.43	nd	0.82	28.3	12.2	0	21.5	0	35.6	2.4	0
YD4-10	1328.75	Shuijingtuo	1.63	nd	2.22	24.8	17.5	0	19.2	0	35.8	2.7	0
YD5-01	587.60	Shuijingtuo	0.98	2.83	0.78	20.7	1.8	0	21.2	6.6	35.7	0	14.0
YD5-02	588.42	Shuijingtuo	0.36	nd	0.67	31.9	3.4	0	40.2	2.5	20.0	1.3	0.7
YD5-07	589.15	Shuijingtuo	0.57	nd	1.12	26.3	2.7	0	40.8	5.8	20.2	3.4	0.8
YD5-04	590.65	Shuijingtuo	1.24	nd	0.98	23.4	0	0	53.3	0	19.4	4.0	0
YD5-05	592.05	Shuijingtuo	1.18	nd	1.34	25.5	0	0	71.6	0	0.0	2.8	0
YD5-06	593.10	Shuijingtuo	1.64	nd	1.76	28.2	0	0	68.4	0	0	3.4	0
YD5-03	595.30	Shuijingtuo	2.40	2.99	3.15	32.7	0	0	64.4	0	0	2.9	0
YD5-08	597.02	Shuijingtuo	3.00	nd	3.01	36.0	0	0	61.7	0	0	2.3	0
YD5-09	599.13	Shuijingtuo	4.64	2.80	1.48	45.3	0	5.2	47.9	0	0	1.6	0
YD5-10	601.95	Shuijingtuo	3.50	nd	3.05	44.6	0	0	53.1	0	0	1.8	0.5

intraparticle pores. These pores occur mainly in clay mineral aggregates, with different shapes and sizes (Fig. 2(i)). Although both interparticle and intraparticle pores in shales can provide a certain amount pore space, their poor connectivity is not conducive to the formation of effective percolation of shale gas, so that their contribution to gas production is low (Wang et al., 2018). The OM pores in the shale samples have a very small size, with an isolated distribution (Fig. 2(f), (h)). For some OM particles, their pores are rare, even between hard pyrite particles (Fig. 2(g)). In addition, the microfractures are mainly shrinkage microfractures formed in the process of dehydration and shrinkage of clay minerals. They usually have a coiled or wisp-like shape, with a short length, which are controlled by the hosted clay mineral aggregates (Fig. 2(j)).

The above differences in the pore development characteristics revealed by the SEM observation between the YD4 and YD5 shale samples are also reflected in their porosity. Overall, the porosity of the YD4 shale samples is larger than that of the YD5 shale samples, with ranges of 0.82–5.01% (an average of 3.54%) and 0.67–3.15% (an average of 1.73%), respectively (Table 1). The porosity of the YD4 shale samples shows a positive correlation with the TOC content ($R^2 = 0.487$) and no obvious relationship with the quartz and clay mineral contents, while the porosity of the YD5 shale samples is significantly positively correlated with clay mineral content ($R^2 = 0.749$), but weakly positively correlated with the TOC and quartz contents, with a R^2 value of 0.388 and 0.331, respectively (Fig. 3). The porosity of the two sets of shale samples is similar when their TOC contents are less than 1% (Fig. 3(a)). This further illustrates that the well-developed OM pores have a significant contribution to the porosity of the YD4 shale samples, while the contribution of the OM pores in the YD5 shale samples to the porosity is limited, and their porosity is also significantly affected by other pore types such as clay minerals and microfractures (Figs. 2(j) and 3(c)). The results are consistent with the Lower Cambrian shale in the northeastern Chongqing area (Meng et al., 2022), but different from the Lower Silurian shale in the Sichuan Basin, where the porosity is strongly positively correlated with the TOC content owing to the more developed OM nanopores (Chen et al., 2021).

3.3. Water saturation and pore structure of shale samples

Based on the water content, porosity, bulk density and grain density of two sets of shale samples, their water saturation was calculated. As shown in Table 2, the water saturation of the YD4 shale samples ranges from 28.40% to 58.20% (an average of 40.11%), while the water saturation of the YD5 shale samples is much greater, ranging from 48.20% to 78.20% (an average of 61.13%).

According to the results of LPCA and LPNA experiments (Table 2), the micropore and mesopore structure parameters of the YD4 shale samples are greater than those of the YD5 shale samples, while their macropore structure parameters are less than those of the YD5 shale samples. For the YD4 shale samples, the micropore specific surface area (SSA_{mic}), mesopore specific surface area (SSA_{mes}) and macropore specific surface area (SSA_{mac}) are 5.62–32.90 m^2/g (an average of 17.47 m^2/g), 3.28–29.30 m^2/g (an average of 14.22 m^2/g) and 0.05–0.09 m^2/g (an average of 0.08 m^2/g), respectively, and the micropore volume (PV_{mic}), mesopore volume (PV_{mes}) and macropore volume (PV_{mac}) are 0.0023–0.0132 cm^3/g (an average of 0.0070 cm^3/g), 0.0042–0.0298 cm^3/g (an average of 0.0150 cm^3/g) and 0.0014–0.0025 cm^3/g (an average of 0.0020 cm^3/g), respectively. For the YD5 shale samples, the SSA_{mic}, SSA_{mes} and SSA_{mac} are 5.62–14.74 m^2/g (an average of 9.41 m^2/g), 0.90–1.77 m^2/g (an average of 1.22 m^2/g) and 0.27–0.59 cm^2/g (an average of 0.46 m^2/g), respectively, and the PV_{mic}, PV_{mes} and PV_{mac} are 0.0025–0.0062 cm^3/g (an average of 0.0043 cm^3/g), 0.0015–0.0055 cm^3/g (an average of 0.0033 cm^3/g) and 0.0045–0.0091 cm^3/g (an average of 0.0075 cm^3/g), respectively.

Fig. 4 presents the relative percentages of the three types of pores in the two sets of shale samples. The SSA of the YD4 shale samples is mainly derived from the micropores, and then mesopores, with only a minor portion of macropores. The relative percentages of SSA_{mic}, SSA_{mes} and SSA_{mac} are respectively 33.75–80.27% (an average of 57.97%), 19.38–66.10% (an average of 41.72%) and 0.08–0.74% (an average of 0.31%) (Fig. 4(a)). The PV of the YD4 shale samples is mainly derived from the mesopores, and the PV_{mes}, PV_{mic} and PV_{mac} account for 33.13–79.42% (an average of

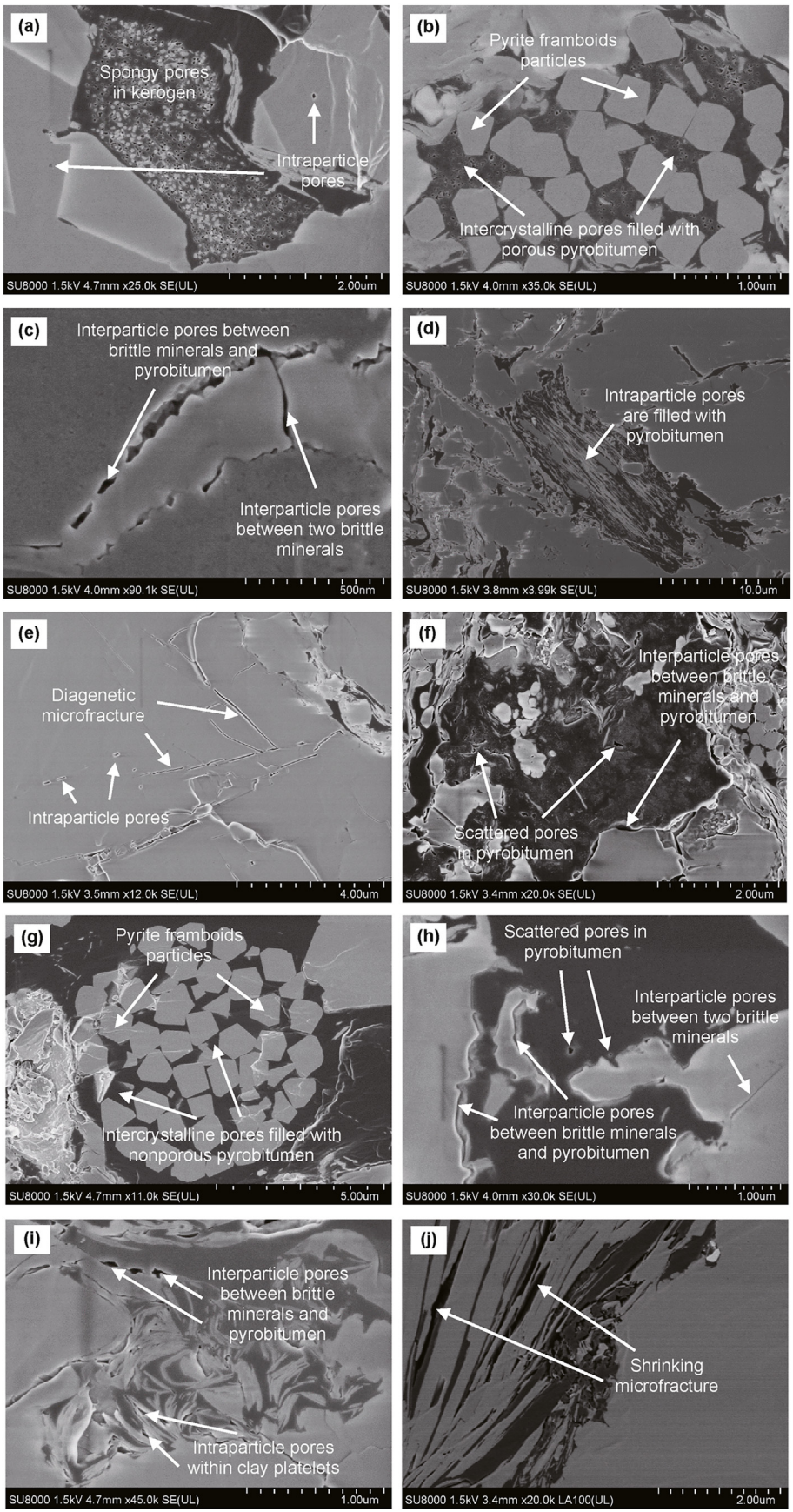

Fig. 2. Pore development characteristics of the studied shale samples revealed by FE-SEM observation. **(a)**–**(e)**: YD4-05 sample, TOC = 6.03%, 1285.65 m; **(f)**–**(j)**: YD5-07 sample, TOC = 2.40%, 595.30 m. **(a)** Kerogen with spongy pores, and dissolution pores inside carbonate minerals. **(b)** Interparticle pores within framboidal pyrite particles, and some of the

58.17%), 15.94–51.81% (an average of 31.30%) and 3.15–19.09% (an average of 10.53%) of the total pore volume (PV_{total}), respectively (Fig. 4(b)). Different from the YD4 shale samples, the micropores and macropores of the YD5 shale samples contribute the most to their SSA_{total} and PV_{total}, respectively, with the relative percentages of 75.94–92.53% (an average of 83.48%), 5.65–16.54% (an average of 11.68%) and 1.82–12.57% (an average of 4.54%) for the SSA_{mic}, SSA_{mes} and SSA_{mac}, respectively (Fig. 4(c)), and 30.00–68.94% (an average of 50.73%), 19.55–40.66% (an average of 28.14%) and 11.52–33.13% (an average of 21.13%) for the PV_{mac}, PV_{mic} and PV_{mes}, respectively (Fig. 4(d)).

3.4. HPMA characteristics

Fig. 5(a) and (b) present the HPMA isotherms of the YD4 and YD5 shale samples at 40 °C. With the increase of pressure, the n_{exc} of each sample rises rapidly, reaching a maximum value in the range of 9–10 MPa, and then decreases and gradually tends to 0, which is similar with previous studies (Pan et al., 2016; Wei et al., 2019; Sun et al., 2022). This is because the difference between the free phase and adsorbed phase methane densities decreases with increasing pressure (Li et al., 2018). In this study, the maximum n_{exc} of the YD4 and YD5 shale samples are 0.79–4.07 cm^3/g (an average of 2.20 cm^3/g) and 0.66–1.26 cm^3/g (an average of 0.88 cm^3/g), respectively (Table 3).

The HPMA parameters of the YD4 and YD5 shale samples are presented in Table 3. For the YD4 shale samples, the n_0, ρ_{ad} and D values are 1.21–5.58 cm^3/g (an average of 3.13 cm^3/g), 0.2599–0.3595 g/cm^3 (an average of 0.2950 cm^3/g) and 0.0069–0.0123 mol^2/kJ^2 (an average of 0.0091 mol^2/kJ^2), respectively. For the YD5 shale samples, the n_0, ρ_{ad} and D values are 1.00–1.82 cm^3/g (an average of 1.31 cm^3/g), 0.2321–0.3139 g/cm^3 (an average of 0.2609 g/cm^3) and 0.0095–0.0172 mol^2/kJ^2 (an average of 0.0130 mol^2/kJ^2), respectively.

Based on the HPMA parameters (n_0, ρ_{ad} and D), Eq. (5) was used to further calculate the n_{ab} value of each sample. As shown in Fig. 5(c) and (d), the variation trend of n_{ab} value with pressure is different from the n_{exc}. The adsorption curve belongs to the Type I adsorption curve (Rouquerol et al., 1994), with an obvious increase in the lower pressure stage and a slow increase in the higher pressure stage.

The HPMA curves of the YD4-01 and YD5-07 samples (their TOC contents are similar, with 2.45% and 2.41%, respectively, see Table 1) at different temperatures (25, 40, 60 and 90 °C) are shown in Fig. 6. These adsorption curves have a similar variation trend at different temperatures, but with a gradually decrease of n_{exc} with increasing temperature, indicating that methane adsorption is an exothermic reaction (Sircar, 1992; Sun et al., 2022). The maximum n_{exc} of the two samples all decreases with the increase of temperatures, ranging from 2.12 cm^3/g to 1.29 cm^3/g and from 0.79 cm^3/g to 0.45 cm^3/g, respectively (Table 4). The methane adsorption parameters between the two samples are also different. The n_0, ρ_{ad} and D values of the YD4-01 sample are 1.96–3.01 cm^3/g, 0.2119–0.3862 g/cm^3 and 0.0084 mol^2/kJ^2, respectively, and the n_0, ρ_{ad} and D values of the YD5-07 sample are 0.75–1.20 cm^3/g, 0.2015–0.2943 g/cm^3 and 0.0131 mol^2/kJ^2, respectively (Table 4).

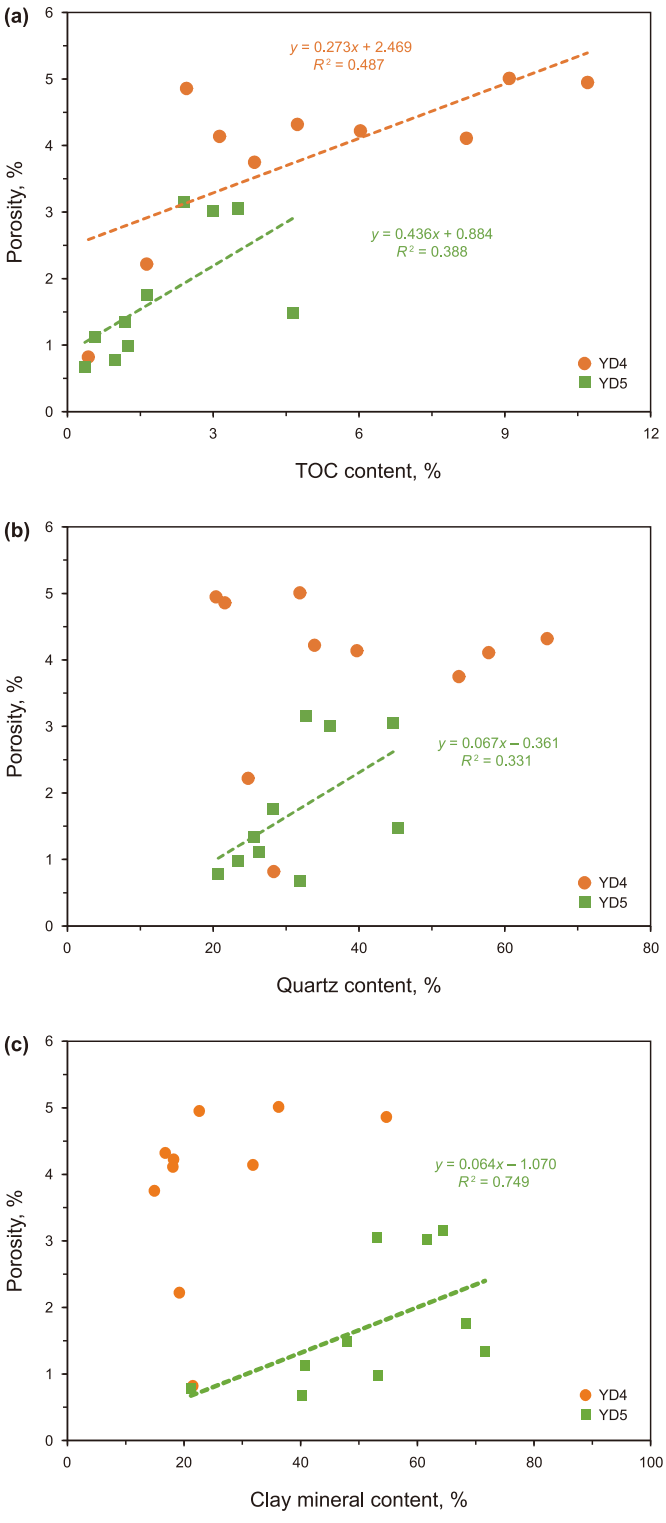

Fig. 3. Cross-plots of porosity versus TOC **(a)**, quartz **(b)** and clay mineral **(c)** contents of the YD4 and YD5 shale samples.

pores are filled with porous OM. **(c)** Pyrobitumen with spongy pores, and interparticle pores occurring between OM and brittle minerals. **(d)** Intraparticle pores within clay minerals filled with OM. **(e)** Diagenetic microfractures resulted from intense compression, and dissolution pores within carbonate minerals. **(f)** Pyrobitumen with scattered pores, and interparticle pores occurring between OM and brittle minerals. **(g)** Intergranular pores within framboidal pyrite particles, and some of the pores are filled with nonporous OM. **(h)** Interparticle pores occurring between OM and brittle minerals and between two brittle minerals. **(i)** Intraparticle pores within clay minerals. **(j)** Shrinking microfractures occurring inside clay mineral.

Table 2
Water content and saturation of the studied shale samples and their bulk density, grain density and pore structure parameters (The data of YD4-01, YD4-02, YD4-06, YD4-07 and YD4-08 samples are from Li et al. (2023a, b)).

Sample	Water content, mg/g	Bulk density, g/cm^3	Grain density, g/cm^3	Water saturation, %	Pore structure parameters							
					SSA_{total}, m^2/g	SSA_{mic}, m^2/g	SSA_{mes}, m^2/g	SSA_{mac}, m^2/g	PV_{total}, cm^3/g	PV_{mic}, cm^3/g	PV_{mes}, cm^3/g	PV_{mac}, cm^3/g
YD4-01	8.95	2.40	2.53	44.20	28.15	14.92	13.16	0.07	0.0217	0.0061	0.0139	0.0017
YD4-02	9.82	2.46	2.50	58.20	27.97	13.86	14.06	0.05	0.0220	0.0056	0.0150	0.0014
YD4-03	4.37	2.79	2.83	32.50	21.77	14.91	6.77	0.09	0.0162	0.0060	0.0081	0.0021
YD4-04	7.39	2.49	2.52	42.60	27.59	19.30	8.20	0.09	0.0199	0.0079	0.0095	0.0025
YD4-05	5.37	2.78	2.83	35.40	26.26	21.08	5.09	0.09	0.0166	0.0086	0.0055	0.0025
YD4-06	6.05	2.73	2.75	40.20	42.13	14.22	27.85	0.06	0.0345	0.0055	0.0274	0.0016
YD4-07	7.12	2.47	2.49	35.10	62.25	32.90	29.30	0.05	0.0444	0.0132	0.0298	0.0014
YD4-08	5.51	2.55	2.59	28.40	54.43	26.35	28.00	0.08	0.0408	0.0100	0.0288	0.0020
YD4-09	7.42	2.54	2.58	38.80	12.24	5.62	6.53	0.09	0.0128	0.0023	0.0081	0.0024
YD4-10	4.01	2.53	2.56	45.70	14.91	11.55	3.28	0.08	0.0110	0.0047	0.0042	0.0021
YD5-01	1.88	2.11	2.69	50.80	7.82	6.33	1.09	0.40	0.0136	0.0028	0.0017	0.0091
YD5-02	1.77	2.23	2.55	58.80	7.03	5.62	1.01	0.40	0.0126	0.0025	0.0015	0.0087
YD5-03	2.91	2.28	2.53	59.20	9.72	8.07	1.06	0.59	0.0128	0.0035	0.0017	0.0076
YD5-04	2.92	2.31	2.59	68.90	9.31	7.07	1.07	1.17	0.0131	0.0031	0.0025	0.0076
YD5-05	4.16	2.42	2.49	75.20	14.90	12.83	1.51	0.56	0.0167	0.0051	0.0038	0.0077
YD5-06	5.51	2.26	2.61	70.80	8.42	6.94	1.21	0.27	0.0150	0.0061	0.0044	0.0045
YD5-07	8.85	2.14	2.50	60.10	10.70	8.63	1.77	0.30	0.0166	0.0035	0.0055	0.0076
YD5-08	8.71	2.16	2.48	62.50	13.48	11.66	1.51	0.31	0.0169	0.0050	0.0049	0.0070
YD5-09	3.26	2.19	2.56	48.20	13.56	12.18	1.10	0.28	0.0162	0.0050	0.0033	0.0079
YD5-10	7.84	2.21	2.58	56.80	15.93	14.74	0.90	0.29	0.0163	0.0062	0.0033	0.0068

4. Discussion

4.1. Controlling factors of shale adsorption capacity

4.1.1. Relationship between n_0 and TOC content

Zhai et al. (2017b) summarized the main factors controlling the enrichment and high yield of marine shale gas in southern China, and believed that the high TOC content and well-developed OM pores of the deep-water shelf shales were the material basis for its shale gas enrichment. Pu et al. (2020) studied the Lower Silurian marine shale in the Sichuan Basin, and found that compared with the shallow-water shelf shale, the deep-water shelf shale has a higher TOC content, a larger effective thickness, and more developed OM pores. In the present study, there is a significant positive correlation between n_0 value and TOC content for the YD4 and YD5 shale samples, and their correlation coefficients (R^2) are as high as 0.736 and 0.745, respectively (Fig. 7), indicating that the TOC content is the main factor affecting the adsorption capacity of the shales, which is consistent with previous studies (Chalmers and Bustin, 2008; Ross and Bustin, 2009; Zhang et al., 2012; Tian et al., 2016).

As shown in Fig. 8, the micropore and mesopore structure parameters of the YD4 shale samples increase with the increase of TOC content, with R^2 ranges of 0.634–0.585 and 0.697–0.688, respectively, while the SSA_{mac} and PV_{mac} have no obvious correlation with the TOC content. The TOC content of YD5 shale samples presents a positive relationship with the SSA_{mic} and PV_{mic} (a R^2 range of 0.507–0.363), but there are no obvious correlations between the TOC content and the mesopore and macropore structure parameters. This is because the OM of the YD4 shale samples mainly develops micropores and mesopores, while the OM pores of the YD5 shale samples are dominated by micropores (Fig. 4). Fig. 9 presents the correlations between the pore structure parameters and n_0 values for the two sets of samples. Its high consistence with Fig. 8 further indicates that the TOC content control on the adsorption capacity of the shales is related to the extremely-developed nanopores of OM compared with the IM and the OM nanopore structure characteristics, and the increase of TOC content will expand the SSA and PV for methane adsorption (Chalmers and Bustin, 2007, 2008; Gasparik et al., 2014; Wei, 2020).

After the TOC content normalization of n_0 (n_0/TOC), it is realized that the adsorption capacity of the YD4 shale samples (an average of 0.413 cm^3/g TOC) is significantly higher than that of the YD5 shale samples (an average of 0.184 cm^3/g TOC). When the TOC content is close to 0, the n_0 values of the two sets of shale samples are basically same (Fig. 7), implying that the IM components are not the main reasons for the differences of methane adsorption capacity between the two sets of shale samples. In addition, Gasparik et al. (2012) studied the adsorption capacities of immature Mesozoic shale and overmature Paleozoic shale (both with high TOC contents and similar clay mineral contents), and found that there was little difference between them; Li et al. (2017) compared the adsorption capacity of various shales, and believed that the adsorption capacity of shale OM changed little with thermal maturity within an EqR_o range of 1.0–3.0% at the same adsorption temperature. Therefore, the adsorption capacity difference between the YD4 and YD5 shale samples is not caused by the difference in their maturity (Table 1).

According to previous studies, the kerogen macerals in the deep-water shelf Lower Cambrian shale in the western Hubei area were mainly derived from saprolite OM, with the kerogen type of I or II_a (Li et al., 2019; Luo et al., 2019a; Shi, 2020; Wei, 2020), while the shallow-water platform Lower Cambrian shale deposited in an oxidizing condition under which the kerogen type would tend to be the type II_b or even type III (Wang, 2018; Xu et al., 2021; Wu et al., 2022). At the low and middle mature stages, type I kerogen has the lowest adsorption capacity, while type III kerogen has the highest adsorption capacity (Zhang et al., 2012). However, at the high and over mature stages, the adsorption capacity of type I kerogen has a significant increase due to the development of a lot of OM pores during the process of oil generation and expulsion, and even exceeds the coal-measure shale (a typical type III kerogen) (Fig. 7).

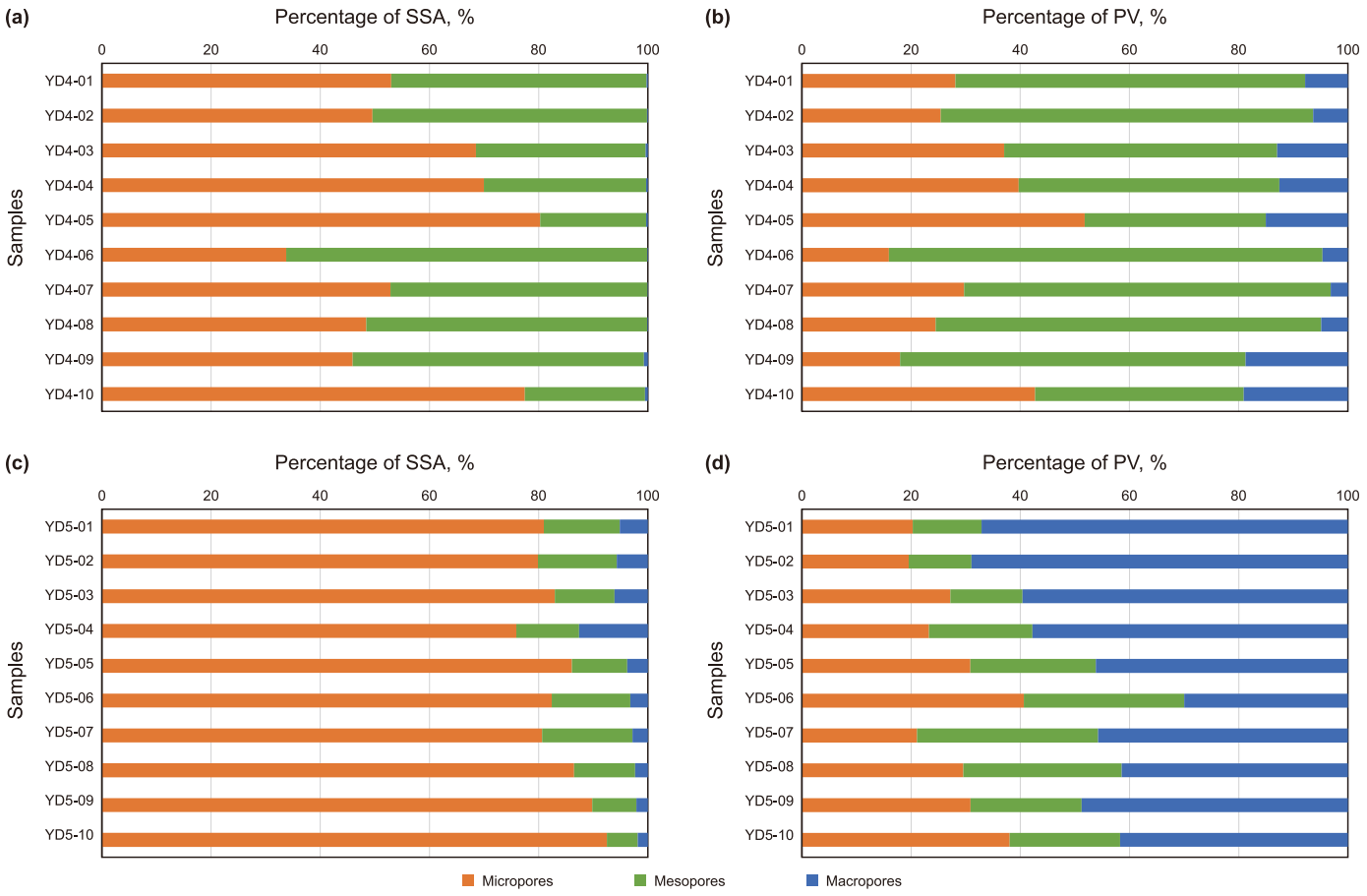

Fig. 4. Relative percentages of pore structure parameters of the three types of pores for the YD4 (**a**, **b**) and YD5 (**c**, **d**) shale samples.

Table 3
The maximum methane excess adsorption capacity and the adsorption parameters obtained from SDR model for the studied shale samples at 40 °C.

Sample	maximum n_{exc}, cm^3/g	n_0, cm^3/g	D, mol^2/kJ^2	ρ_{ad}, g/cm^3
YD4-01	1.69	2.42	0.0084	0.2904
YD4-02	1.72	2.55	0.0103	0.2862
YD4-03	1.11	1.60	0.0090	0.2794
YD4-04	2.45	3.53	0.0089	0.3325
YD4-05	1.46	2.09	0.0082	0.3174
YD4-06	3.75	5.33	0.0080	0.3595
YD4-07	4.07	5.58	0.0075	0.2723
YD4-08	3.61	4.91	0.0069	0.2599
YD4-09	0.79	1.21	0.0123	0.2924
YD4-10	1.37	2.03	0.0110	0.2602
YD5-01	0.70	1.08	0.0143	0.2595
YD5-02	0.66	1.07	0.0167	0.2358
YD5-07	0.62	1.00	0.0150	0.2723
YD5-04	0.66	1.09	0.0172	0.2824
YD5-05	1.00	1.47	0.0095	0.3139
YD5-06	0.85	1.26	0.0106	0.2951
YD5-03	0.76	1.12	0.0131	0.2355
YD5-08	1.10	1.49	0.0120	0.2321
YD5-09	1.26	1.82	0.0106	0.2484
YD5-10	1.20	1.74	0.0107	0.2337

Based on the comparison results in Fig. 7, the adsorption capacity of the YD4 shale samples is comparable to that of the deep-water shelf Lower Cambrian shale from other areas in southern China reported by previous studies, but the adsorption capacity of the YD5 shale samples is even less than that of the coal-measure shale. Therefore, it is speculated that the difference in kerogen types should be another major reason responding for the difference in adsorption capacity between the YD4 and YD5 shale samples. However, since the YD4 and YD5 shale samples are in the over mature stage, further work is needed to determine the original OM properties under the two sedimentary facies.

4.1.2. Relationship between n_0 and clay mineral content

The effect of clay mineral contents on the adsorption capacity of the YD4 and YD5 shale samples is different significantly. For the former, there is no obvious relationship between the n_0 value and clay mineral content, while for the latter, there is a weak positive correlation between the n_0 value and clay mineral content ($R^2 = 0.124$) (Fig. 10). This indicates that compared with the YD4 shale samples, the clay mineral content of the YD5 shale samples has a relatively greater contribution to their adsorption capacity, although this effect is much less than that of TOC content. This observation can be explained by their pore structure characteristics related to their clay minerals and OM.

Ji et al. (2012a) compared the adsorption capacity of different clay minerals using the HPMA experiments, and believed that illite had the lowest adsorption capacity, with a maximum adsorption capacity of 1.72 mL/g, which was less than montmorillonite (8.12 mL/g) and kaolinite (2.70 mL/g), and similar to chlorite (1.81 mL/g). It is generally believed that the adsorption capacity of

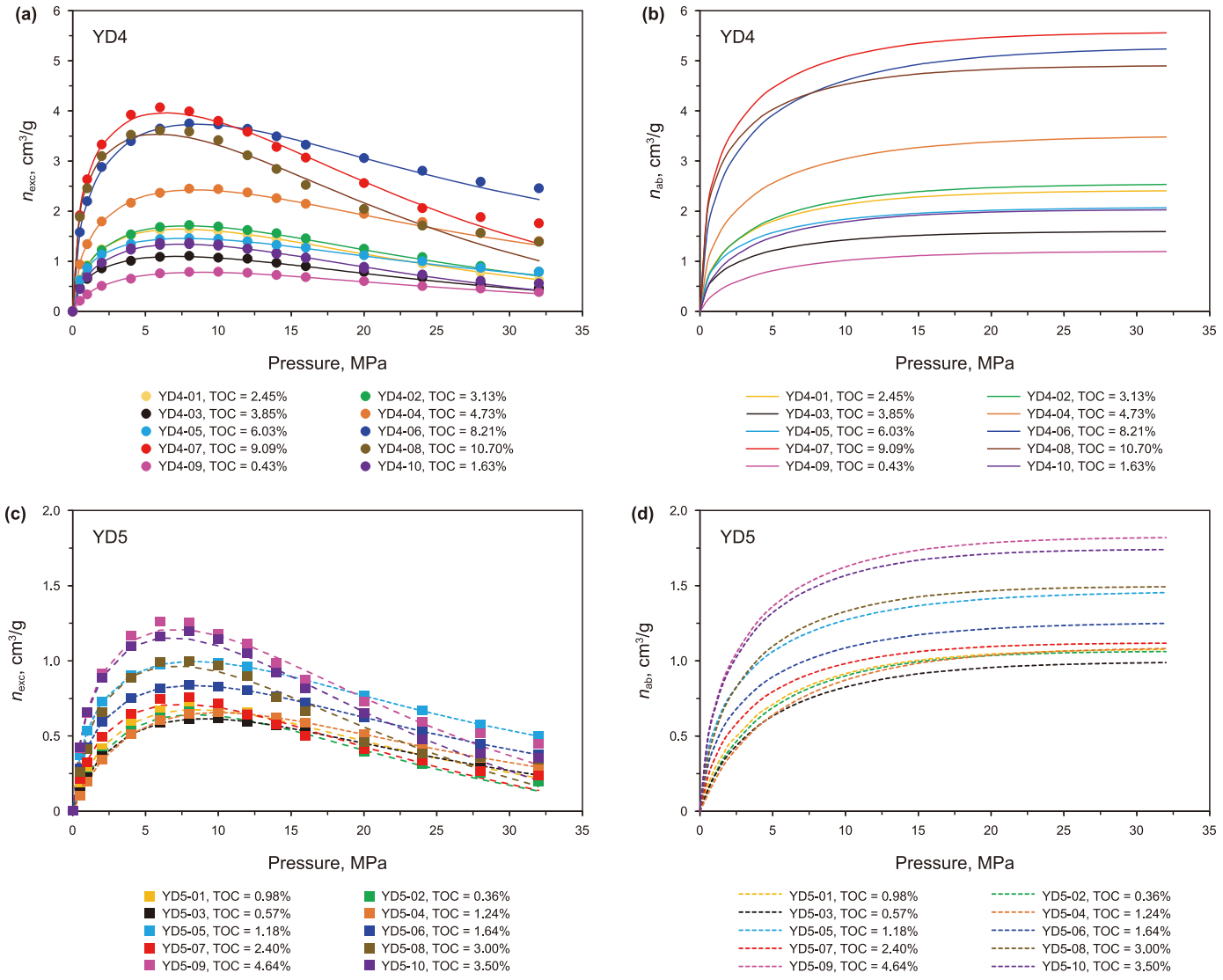

Fig. 5. Methane excess adsorption the YD4 **(a)** and YD5 **(b)** shale samples and methane absolute adsorption isotherms of the YD4 **(c)** and YD5 **(d)** shale samples using the SDR fitting model at 40 °C.

clay minerals depends on their internal structure, the size of pores between crystal layers, as well as the porosity and SSA of their aggregates (Cheng and Huang, 2004; Ross and Bustin, 2009). Illite has a three-layer structure, with the potassium ions locating between the upper and lower crystal layers, and its adsorption site is mainly interlamellar pores, which results in a small SSA (only 30 m^2/g) (Ji et al., 2012a) and a low adsorption capacity. In the YD4 and YD5 shale samples, their clay mineral is mainly illite. For the YD4 shale samples, there is no obvious relationship between the pore structure parameter and clay mineral content (Fig. 11(a) and (b)), which is related to the higher TOC content, and the much greater adsorption capacity of OM than that of clay minerals (Ji et al., 2012b; Rexer et al., 2014; Li et al., 2018), consequentially masking the contribution of clay minerals to the pore structure, and also to the absorption capacity (Fig. 10). For the YD5 shale samples, the micropore and mesopore structure parameters are positively correlated to the clay mineral content, with R^2 ranges of 0.255–0.313 and 0.419–0.634, respectively (Fig. 11(c) and (d)), indicating that the clay mineral provides a relatively greater contribution to the nanopores, especially for the micropores and mesopores, which is consistent with the SEM observation (Fig. 2(i)).

4.1.3. Relationship between adsorption parameters and temperature

As shown in Fig. 12, the n_0 values of the samples YD4-01 and YD5-07 decrease with the increase of temperatures, with a strong negative correlation (R^2 = 0.802 and 0.948, respectively), which is consistent with the Li et al. (2017). The slopes of their linear regression equations are −0.014 cm$^3\cdot$ g$^{-1}\cdot$°C^{-1} for the YD4-01 and −0.007 cm$^3\cdot$ g$^{-1}\cdot$°C^{-1} for the YD5-07, suggesting that the weakening effect of temperatures on the adsorption capacity of the YD4-01 is stronger than that of the YD5-07. The ρ_{ad} values of the two samples also present an obvious negative correlation with the temperature (R^2 = 0.855 and 0.812, respectively), with the linear regression equation slopes of −0.002 cm$^3\cdot$ g$^{-1}\cdot$°C^{-1} for the YD4-01 and −0.001 cm$^3\cdot$ g$^{-1}\cdot$°C^{-1} for the YD5-07 (Fig. 12). This is because a higher temperature will expand the distance between the adsorbed methane molecules (Zhou et al., 2000; Rexer et al., 2014; Sun et al.,

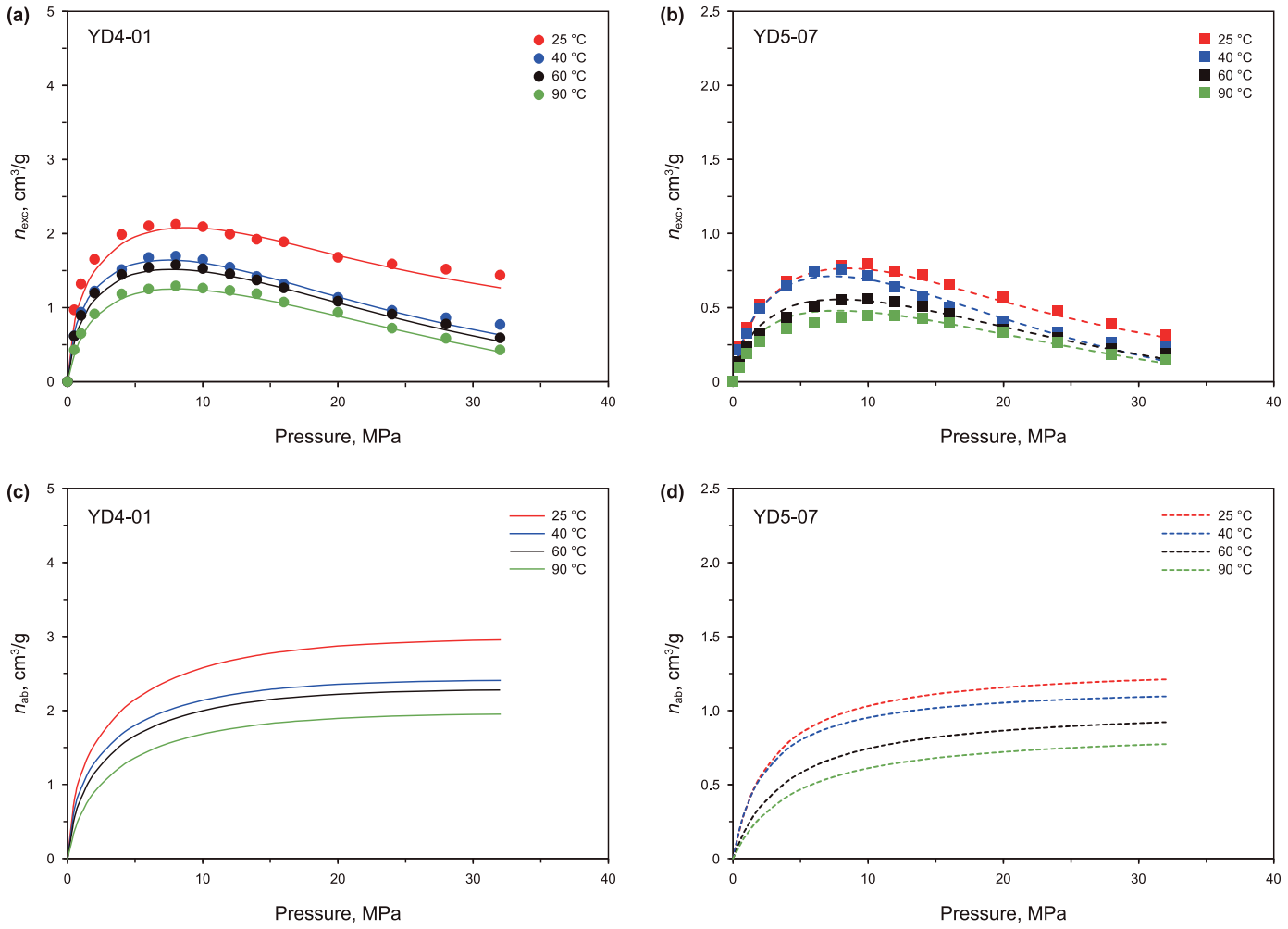

Fig. 6. Methane excess adsorption isotherms of the YD4-01 **(a)** and YD5-07 **(b)** samples and methane absolute adsorption isotherms of the YD4-01 **(c)** and YD5-07 **(d)** samples at different temperatures.

Table 4
The maximum methane excess adsorption capacity and the adsorption parameters obtained from SDR model for the studied two shale samples at different temperatures.

Sample	Temperature, °C	Maximum n_{exc}, cm³/g	n_0, cm³/g	D, mol²/kJ²	ρ_{ad}, g/cm³
YD4-01	25	2.12	3.01	0.0084	0.3862
	40	1.69	2.33		0.2904
	60	1.58	2.29		0.2482
	90	1.29	1.96		0.2119
YD5-07	25	0.79	1.20	0.0131	0.2943
	40	0.76	1.12		0.2355
	60	0.56	0.87		0.2295
	90	0.45	0.75		0.2015

2022). This result also indicates that the type I-II$_a$ kerogen would be more strongly affected by the adsorption temperature than the type II$_b$-III kerogen in the over mature stage.

4.2. Geological models of GIP

4.2.1. GIP content models

According to previous studies, the main burial depth of the Lower Cambrian shale is between 1000 m and 5500 m in the western Hubei area, and the current surface temperature and

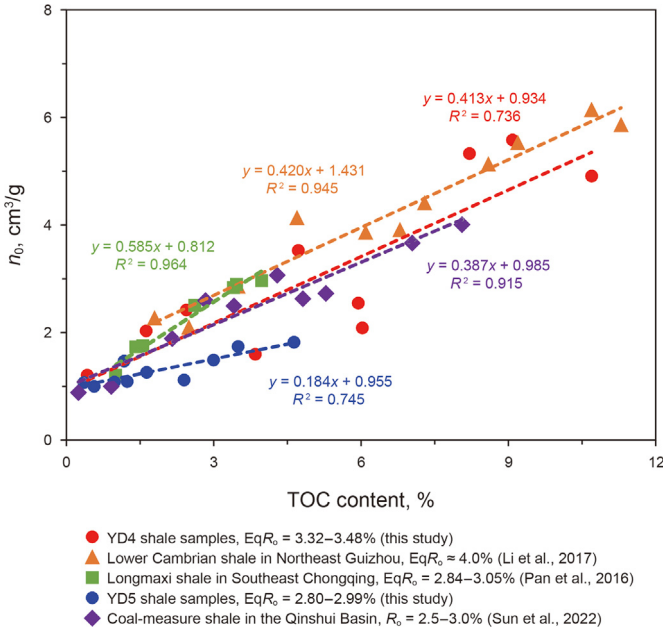

Fig. 7. Cross-plot of n_0 values versus TOC contents of different shale samples at 40 °C.

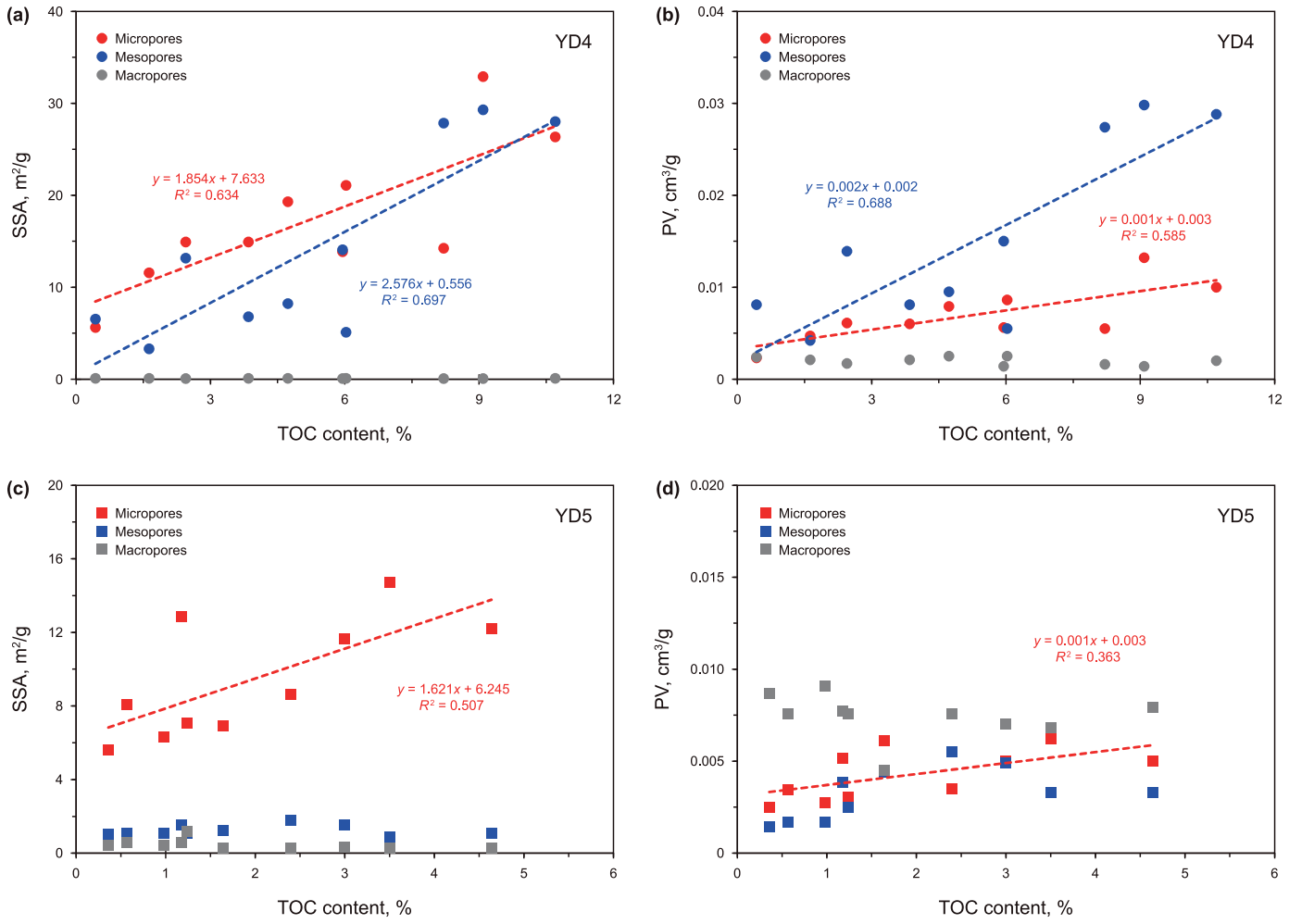

Fig. 8. Cross-plots of pore structure parameters versus TOC contents of the YD4 **(a, b)** and YD5 **(c, d)** shale samples.

geothermal gradient of the area are about 15 °C and 22 °C/km, respectively (Fang et al., 2022; Li et al., 2022a; Wang et al., 2022). In the Sichuan Basin and its nearby areas, the formation pressure coefficient (PC) of marine shale gas reservoirs is generally 1.0–2.0 (Zhao et al., 2016; Zhou et al., 2016). Combining these geological parameters with the data of the YD4-01 and YD5-07 samples such as the bulk density (2.40 g/cm^3 and 2.27 g/cm^3, respectively), water saturation (44.2% and 60.1%, respectively), porosity (4.86% and 3.15%, respectively) and methane adsorption parameters (Table 3), their free, adsorbed and total gas contents at different burial depths were calculated by Eqs. (7)–(9). The GIP content models based on the two samples were proposed (Fig. 13).

For GIP model of the YD4-01, the free gas content continually increases with increasing burial depth, but the adsorbed gas content increases rapidly at the burial depth of <500 m, and reaches a maximum value (2.30–2.49 cm^3/g) between 800 m and 1200 m, and then gradually decreases with the further increase of burial depth (Fig. 13(a)). This variation trend of GIP content is similar to the models from Tang et al. (2016) and Tian et al. (2016), implying that the adsorbed gas content is mainly affected by pressure when the burial depth is shallow, while it is mainly controlled by temperature at the deep burial condition (Hao et al., 2013). The GIP model of the YD5-07 is also similar to that of the YD4-01, but with quite low free and adsorbed gas contents (Fig. 13(b)). For the two models, the relative proportions of free and adsorbed gas contents in the total gas content change opposite with the burial depth. With the increase of burial depth, the proportion of free gas content increases, while that of adsorbed gas content decreases (Fig. 14). Therefore, the conversion of free gas to adsorbed gas occurs during strata uplift and denudation. According to Figs. 13 and 14, the shale reservoir is dominated by adsorption gas at a shallow depth, and the free gas will exceed the adsorption gas at some a depth which is variable, depending on not only the properties of shales themselves, but also the geological conditions, especially the PC.

A high pore pressure can significantly increase the free gas content in shales because the gas density is positively correlated to the pressure, which leads to the enhancement of gas storage capacity in a certain pore space (Wei, 2020). However, the effect of pore pressure on the adsorbed gas content is small, especially at a deep burial depth condition. Taking the burial depth of 5000 m as an example for the studied shale samples, when PC decreases from 2.0 to 1.0, the free and adsorbed gas contents of the YD4-01 decrease by 0.92 cm^3/g and 0.01 cm^3/g, respectively, while those of the YD5-07 decrease by 0.32 cm^3/g and 0.01 cm^3/g, respectively (Fig. 13). Therefore, the proportion of free gas content will increase with the increase of pore pressure. For instance, when at a depth of 3000 m and PC values of 1.0, 1.5 and 2.0, respectively, the relative percentages of free gas content of the YD4-01 are 36.12%, 43.94% and 49.22%, respectively, and those of the YD5-07 are 54.60%, 61.19% and 65.43%, respectively (Fig. 14). The differential influence of pore pressure on free and adsorbed gases is vital for evaluating the contribution of different shale gas phases to gas production. In the early stage of shale gas

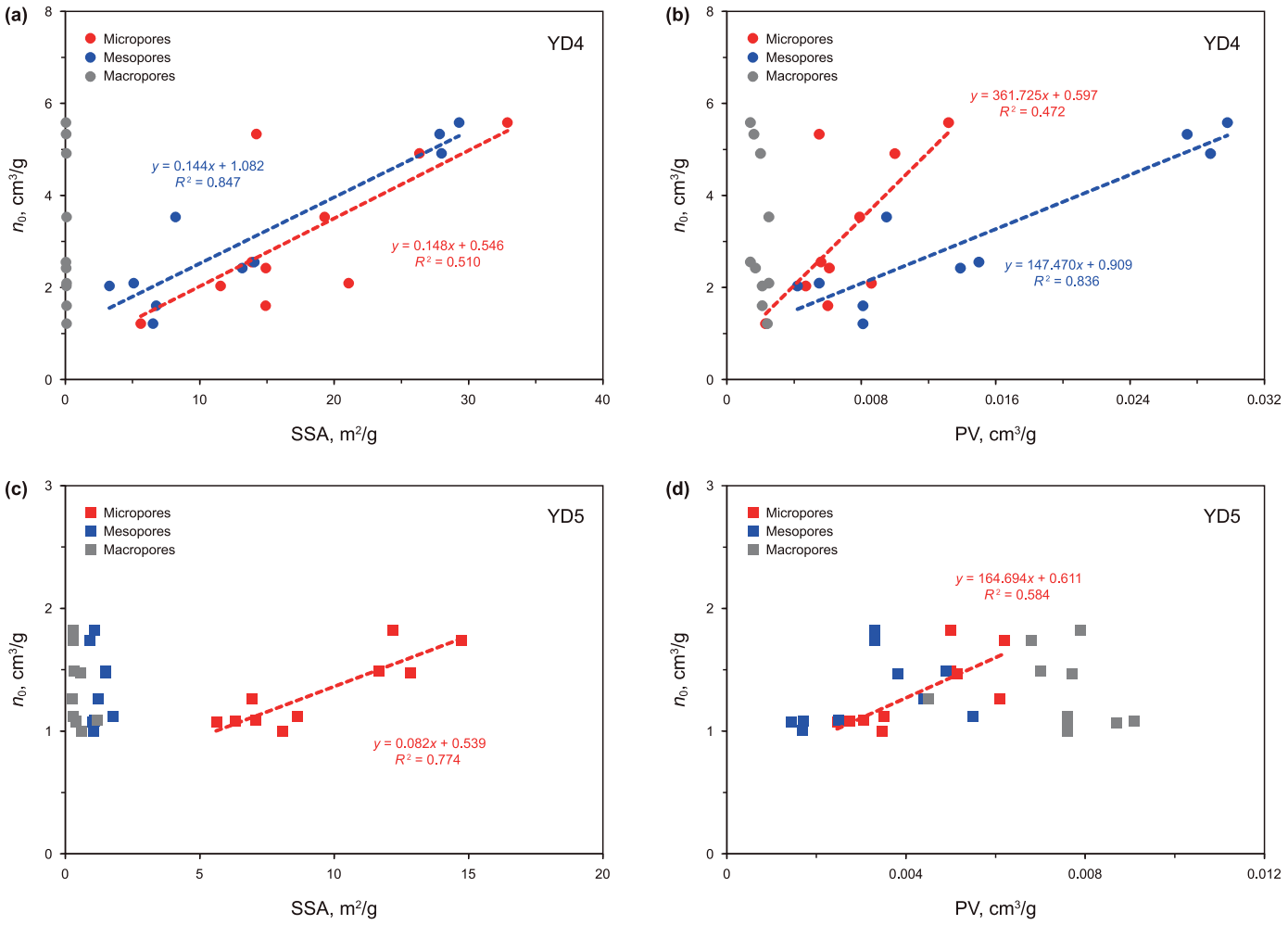

Fig. 9. Cross-plots of n_0 values versus pore structure parameters of the YD4 **(a, b)** and YD5 **(c, d)** shale samples.

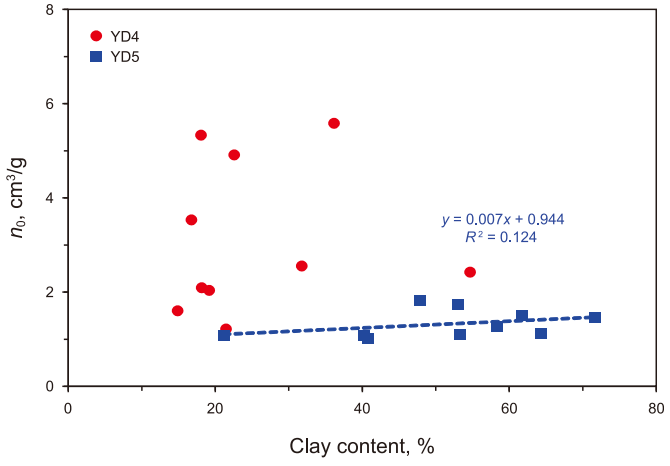

Fig. 10. Cross-plot of n_0 values versus clay contents of the YD4 and YD5 shale samples.

exploitation, the pore pressure of shale gas reservoir decreases rapidly, and abundant free gas is released rapidly, while almost no adsorbed gas in the shale matrix is desorbed. At this period, the shale gas yield is dominated by the free gas, with little contribution from the adsorbed gas (Wei et al., 2019).

Based on the GIP content models in Fig. 13, although the TOC contents of the two typical samples are similar (2.45% and 2.40% for the YD4-01 and YD5-07 samples, respectively), their GIP contents are quite different. For the YD4-01 model, the GIP content does not exceed 2 m^3/t at the burial depth of <200–300 m under the three PC conditions, and can be as high as 3–4 m^3/t at the burial depth of >2000 m. For the YD5-07 model, the GIP content is generally less than 1.0 m^3/t, and does not exceed 1.5 m^3/t at any conditions. A GIP content of 2.0 m^3/t is generally regarded as the low limit standard of shale gas reservoirs with commercial development potential (Wang et al., 2012; Xiao et al., 2015). Referred to this standard, the deep-water shelf shale represented by the YD4-01 sample has a good exploration and development potential, while the shallow-water platform shale represented by the YD5-07 sample basically has no shale gas potential.

4.2.2. *Influence of porosity and water saturation on free gas content*

The porosity and water saturation have a great influence on the free gas content of shales (Cheng, et al., 2022; Sun et al., 2022), and they vary widely for the shale samples from the Wells YD4 and YD5 (Tables 1 and 2). Therefore, a further investigation was conducted

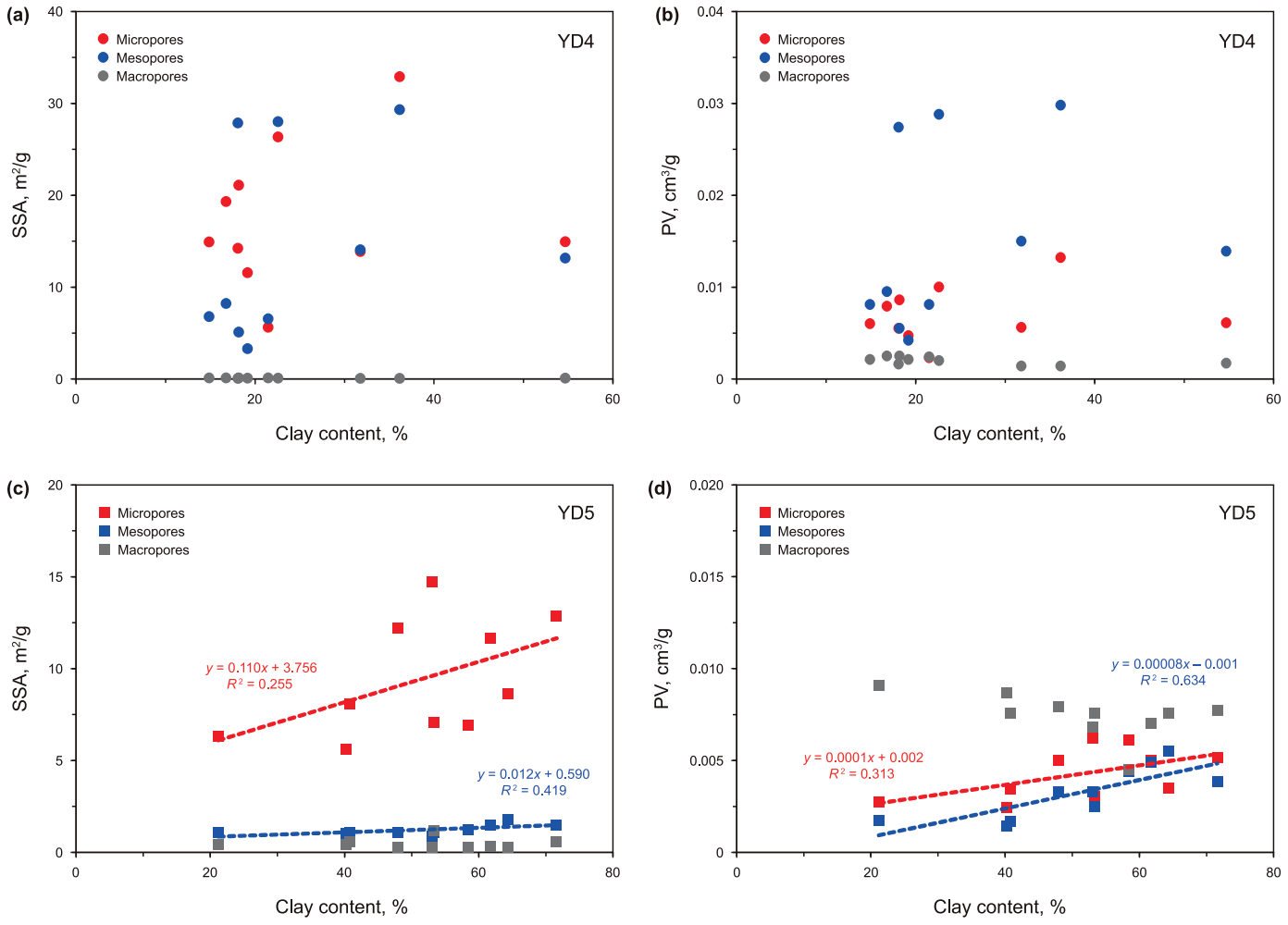

Fig. 11. Cross-plots of pore structure parameters versus clay contents of the YD4 **(a, b)** and YD5 **(c, d)** shale samples.

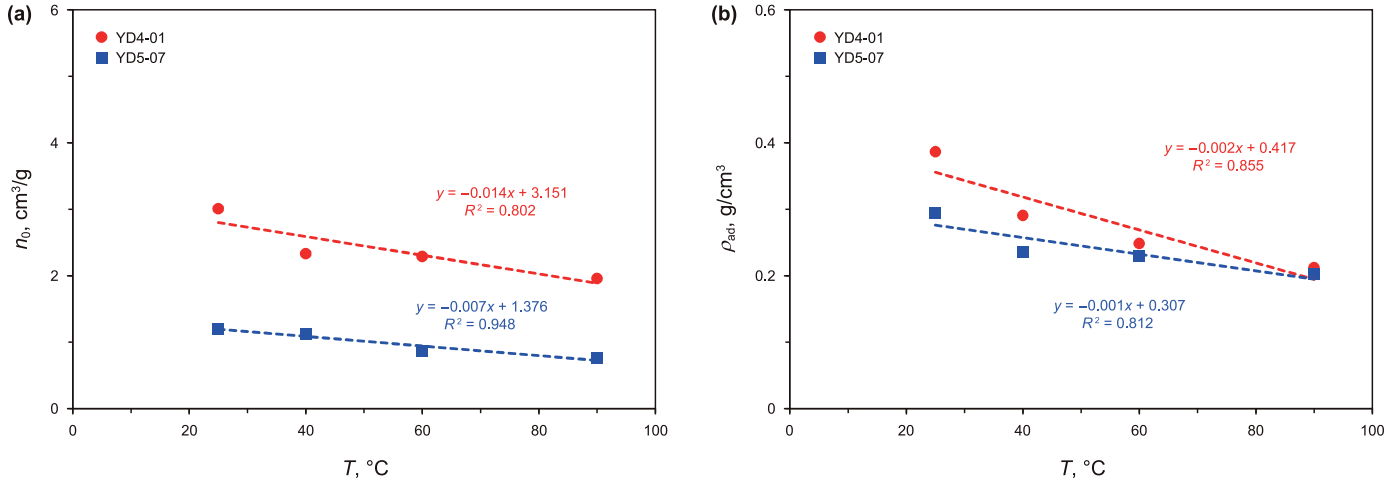

Fig. 12. Cross-plots of n_0 **(a)** and ρ_{ad} **(b)** values of the YD4-01 and YD5-07 samples versus adsorption temperatures.

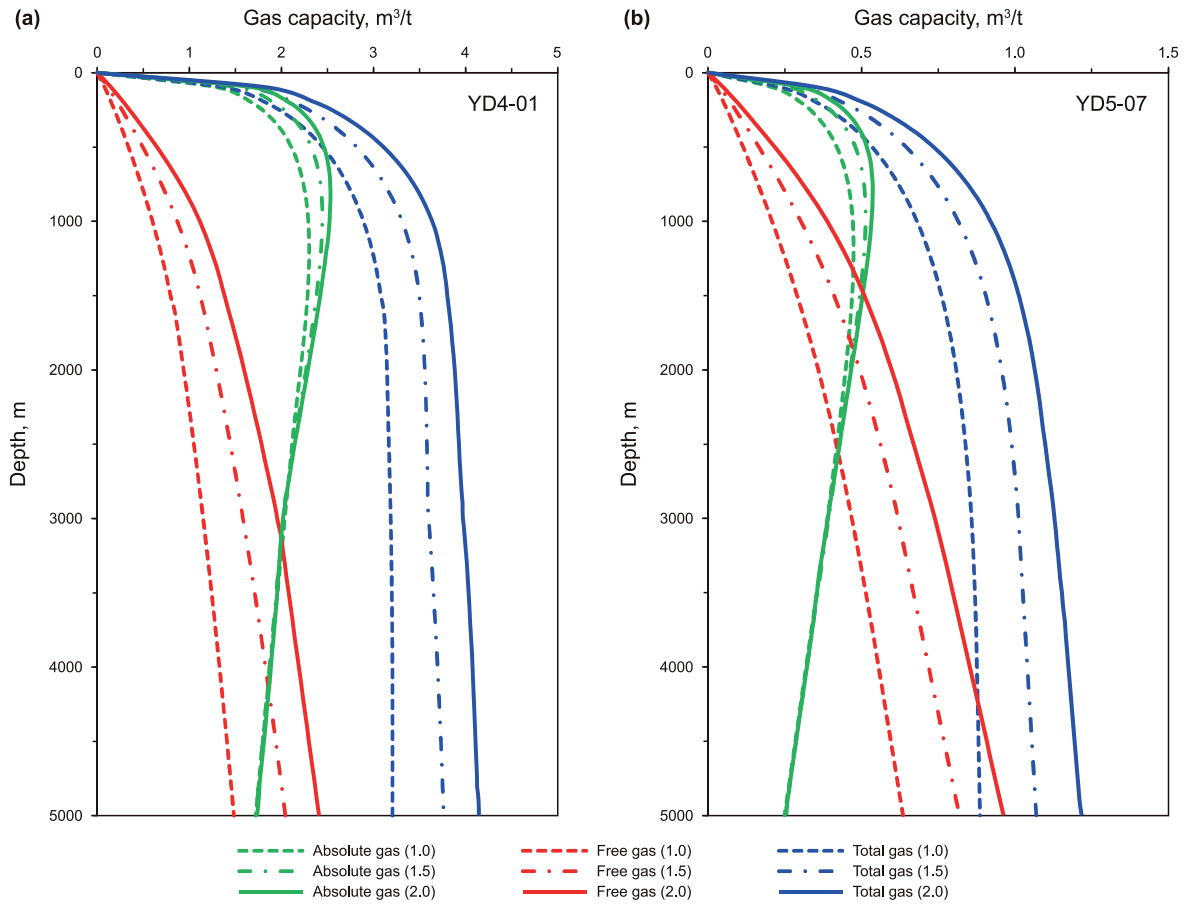

Fig. 13. GIP content models based on the YD4-01 **(a)** and YD5-07 **(b)** samples at different pressure coefficients.

for the two samples (YD4-01 and YD5-07) as the porosity varies from 1% to 6% or the water saturation changes from 10% to 70%.

According to Fig. 15, the greater porosity obviously increases the free gas contents of the YD4-01 and YD5-07 samples, and the free gas content of the YD4-01 sample is much higher than that of the YD5-07 sample under the same porosity and PC conditions. Taking the buried depth of 5000 m as an example, with increasing the porosity from 1% to 6%, the corresponding free gas contents increase from 0.50 m^3/t to 1.83 m^3/t (PC = 1.0), from 0.85 m^3/t to 2.33 m^3/t (PC = 1.5), and from 1.10 m^3/t to 2.84 m^3/t (PC = 2.0) for the YD4-01 sample (Fig. 15(a)–(c)), while the corresponding free gas contents increase from 0.40 m^3/t to 1.15 m^3/t (PC = 1.0), from 0.56 m^3/t to 1.27 m^3/t (PC = 1.5), and from 0.65 m^3/t to 1.47 m^3/t (PC = 2.0) for the YD5-07 sample (Fig. 15(d)–(f)).

As shown in Fig. 16, the greater water saturation significantly decreases the free gas contents of the YD4-01 and YD5-07 samples, and the free gas content of the YD4-01 sample is much higher than that of the YD5-07 sample under the same water saturation and PC conditions. Taking the buried depth of 5000 m as an example, with increasing the water saturation from 10% to 70%, the corresponding free gas contents decrease from 3.33 m^3/t to 0.47 m^3/t (PC = 1.0), from 4.19 m^3/t to 0.66 m^3/t (PC = 1.5), and from 4.80 m^3/t to 1.17 m^3/t (PC = 2.0) for the YD4-01 sample (Fig. 16(a)–(c)), and the corresponding free gas contents decrease from 1.58 m^3/t to 0.47 m^3/t (PC = 1.0), from 1.80 m^3/t to 0.66 m^3/t (PC = 1.5), and from 2.11 m^3/t to 0.78 m^3/t (PC = 2.0) for the YD5-07 sample (Fig. 16(d)–(f)).

5. Geological implications

Chen et al. (2018) studied the Early Cambrian paleoenvironment in the western Hubei area, and found that the deep-water shelf seawater was stratified, sulfide and anoxic, which was very conducive to the deposition and preservation of OM, providing a good material basis for the enrichment of shale gas. Therefore, it is considered that the deep-water shelf facies is favorable to the development of the Lower Cambrian organic-rich shale in this area. In the last few years, the shale gas drilling results have also showed that the wells with a high GIP content all locate in the deep-water shelf and the adjacent slope facies, while the shallow-water platform facies shale has generally a very low GIP content (Luo et al., 2020).

The difference of shale gas contents between the deep-water shelf and shallow-water platform facies in the western Hubei area can be partly explained by the GIP content models proposed in the present study. According to the results from the present study, the GIP content of deep-water shelf shale in the western Hubei area should be obviously higher than that of shallow-water platform shale even under the same PC, porosity, water saturation and burial depth conditions, for which the essential reason is that the deep-water shelf facies shale has a higher TOC content and a better kerogen type, which leads to more-developed OM pores. Moreover, the available data have also documented that the Lower Cambrian Shuijingtuo Formation shale in the deep-water shelf facies area is

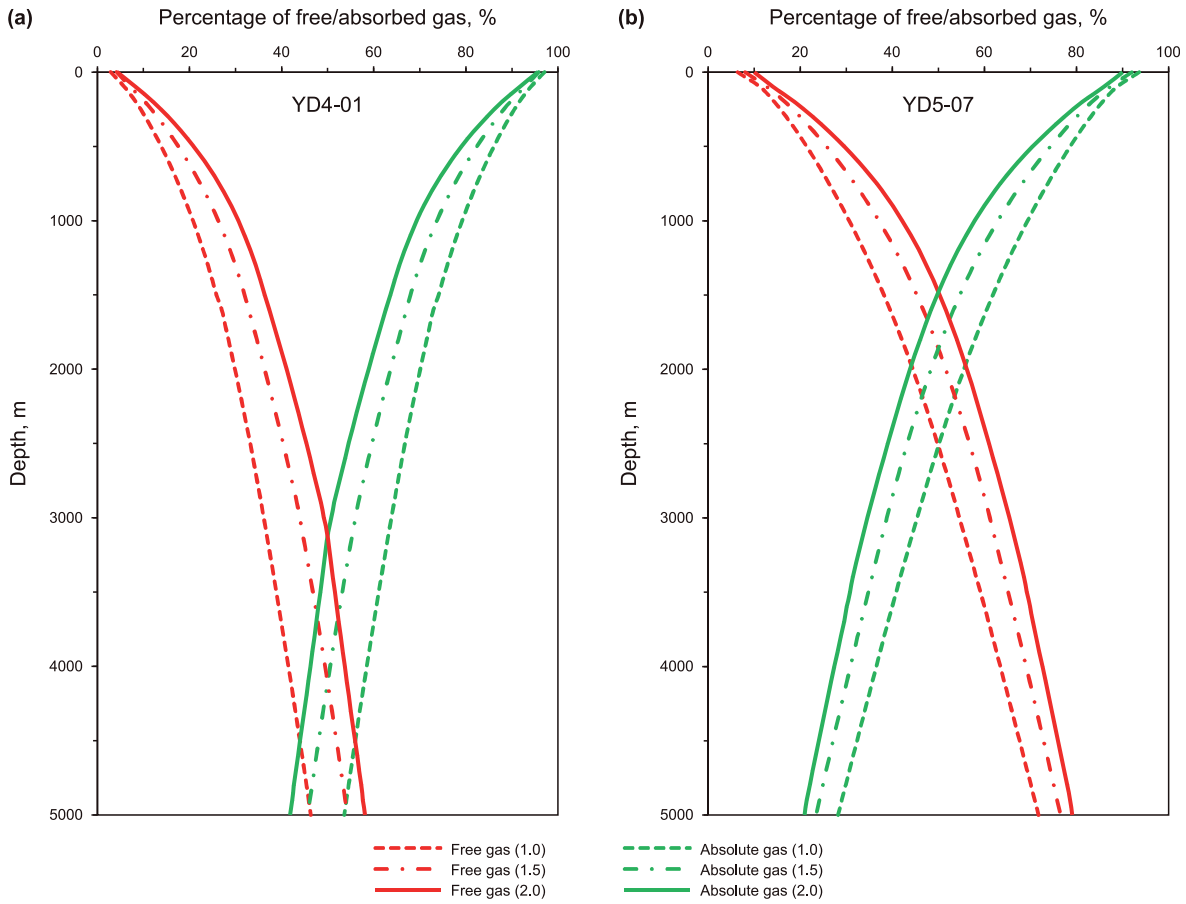

Fig. 14. Changes in relative percentages of free and adsorbed gases with burial depth for the YD4-01 and YD5-07 samples at different pressure coefficients.

about 80–150 m thick, an average TOC content of >2.0%, a maturity of <3.5% EqR_o, a porosity range mainly between 2% and 5% and a water saturation of 30–60% (Luo et al., 2019a; Li et al., 2022a; Zhang et al., 2023), with a great hydrocarbon generation potential and a good storge condition of shale gas. These factors together determine that the deep-water shelf shale is the favorable facies for the formation of Lower Cambrian shale gas play in the western Hubei area, to which a great attention should be paid for further exploration and development.

It should be pointed out that the deep-water shelf and shallow-water platform facies in the studied region develop around the Huangling uplift, both with a weak structural deformation (Luo et al., 2020; Zhai et al., 2020), so the preservation conditions would be not the main reason for the difference of GIP contents between the two facies shales. However, the structural deformation has undeniably a significant effect on shale gas preservation, and it should be also considered for the Lower Cambrian shale gas reservoirs located at different structural belts.

6. Conclusions

Through studying the differences of pore types, nanopore structure and adsorption performance of the Lower Cambrian shales from the deep-water shelf and shallow-water platform facies in the western Hubei area, South China, the following conclusions are obtained.

(1) The deep-water shelf shale mainly develops OM pores, while the shallow-water platform shale mainly develops IM pores. The SSA and PV of the deep-water shelf shale mainly come from micropores and mesopores, respectively, while those of the shallow-water platform shale are mainly from micropores and macropores, respectively.

(2) The methane adsorption capacity of deep-water shelf shale is significantly higher than that of the shallow-water platform shale, with the maximum absolute adsorption capacity of 1.21–5.58 cm^3/g (an average of 3.13 cm^3/g) and 1.00–1.82 cm^3/g (an average of 1.31 cm^3/g), respectively. The differences in their TOC contents and kerogen types are the most important factors responsible for the difference in their adsorption capacity.

(3) The shale GIP geological models further show that the deep-water shelf facies is a favorable target for the Lower Cambrian shale gas exploration due to the high GIP content and great shale thickness, while the shallow-water platform facies shale has a low GIP content, without shale gas potential.

Declaration of competing interest

The authors declare that they have no known competing financial interests or personal relationships that could have appeared to influence the work reported in this paper.

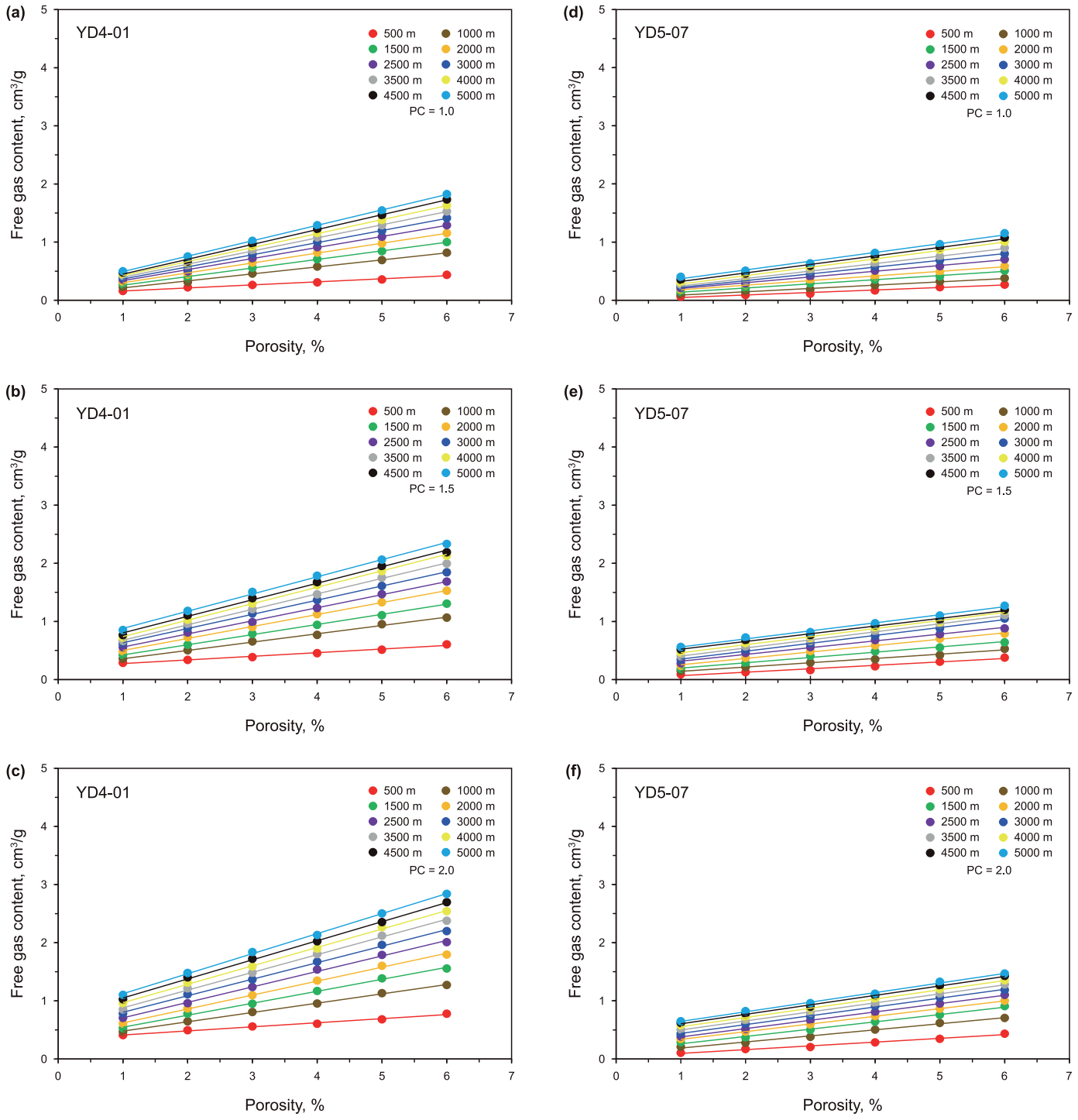

Fig. 15. Cross-plots of free gas content versus porosity under different burial depths and pressure coefficients for the YD4-01 (**a**–**c**) and YD5-07 (**d**–**f**) samples with the water saturation of 50%.

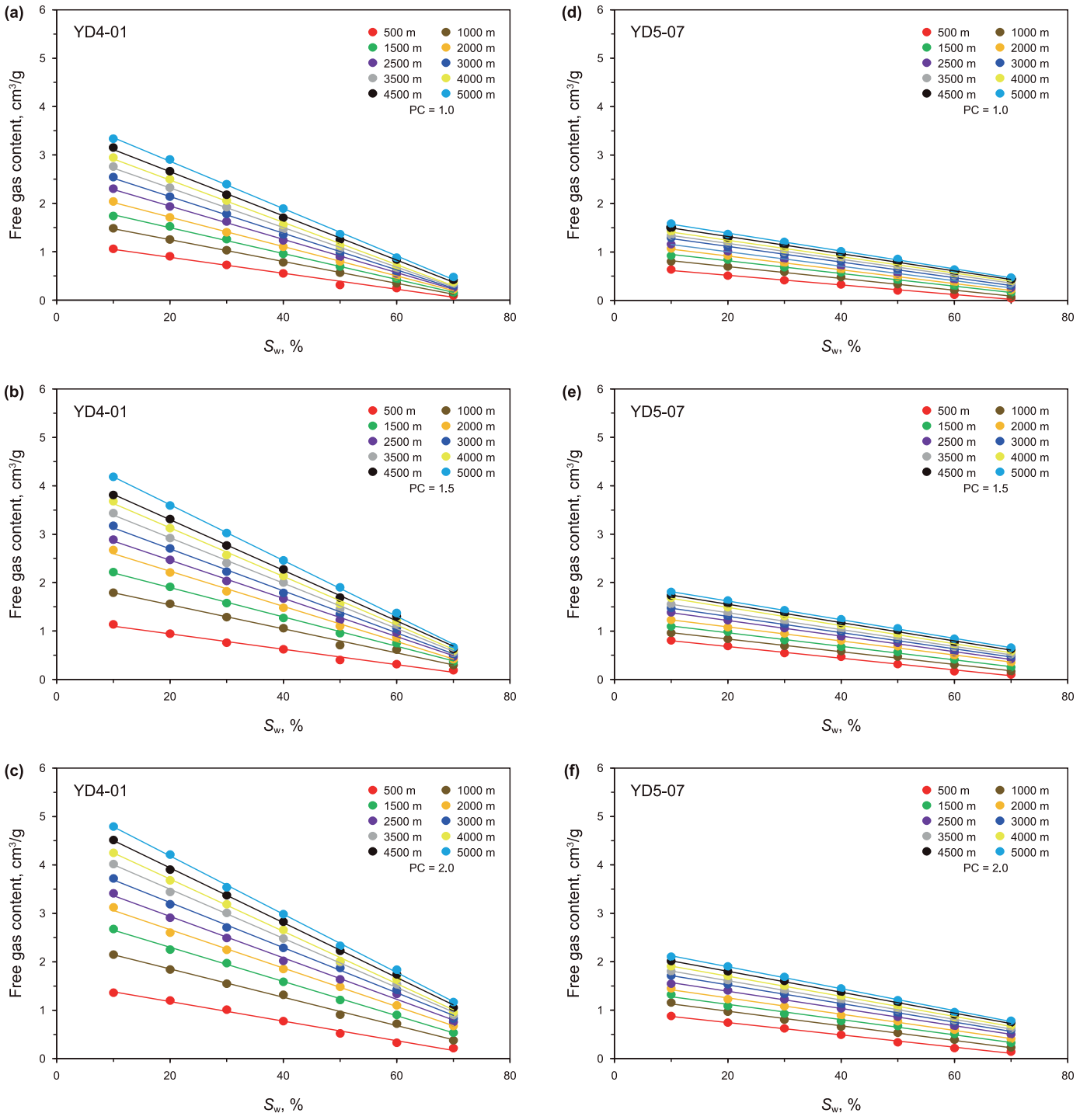

Fig. 16. Cross-plots of free gas content versus water saturation under different burial depths and pressure coefficients for the YD4-01 **(a–c)** and YD5-07 **(d–f)** samples (their porosity was set to be 4%).

Acknowledgments

This research was financially supported by the National Natural Science Foundation of China (Grant Nos. 42030804 and 42330811), and the "Deep-time Digital Earth" Science and Technology Leading Talents Team Funds for the Central Universities for the Frontiers Science Center for Deep-time Digital Earth, China University of Geosciences (Beijing) (Fundamental Research Funds for the Central Universities; Grant No. 2652023001). The authors appreciate both editors and reviewers for their precious time and insightful comments and suggestions that greatly improved the manuscript.

References

Bae, J.S., Bhatia, S.K., 2006. High-pressure adsorption of methane and carbon dioxide on coal. Energy Fuels 20, 2599–2607. https://doi.org/10.1021/ef060318y.

Cheng, P., Xiao, X.M., Tian, H., Wang, X., 2018. Water content and equilibrium saturation and their influencing factors of the Lower Paleozoic overmature organic-rich shales in the Upper Yangtze region of Southern China. Energy Fuels 32, 11452–11466. https://doi.org/10.1021/acs.energyfuels.8b03011.

Chen, X.H., Wei, K., Zhang, B.M., Li, P.J., Li, H., Liu, A., Luo, S.Y., 2018. Main geological factors controlling shale gas reservoir in the Cambrian Shuijingtuo Formation in Yichang of Hubei Province as well as its and enrichment patterns. Chin. Geol. 45 (2), 207–226. https://doi.org/10.12029/gc20180201 (in Chinese).

Chen, J., Xu, Y.H., Gai, H.F., Xiao, Q.L., Wen, J.Z., Zhou, Q., Li, T.F., 2021. Understanding water accessibility and pore information of overmature marine shales using water vapor sorption. Mar. Petrol. Geol. 130, 105120. https://doi.org/10.1016/j.marpetgeo.2021.105120.

Chalmers, G.R.L., Bustin, R.M., 2008. Lower Cretaceous gas shales in northeastern British Columbia, part 1: geological controls on methane sorption capacity. Bull. Can. Petrol. Geol. 56, 1–21. https://doi.org/10.2113/gscpgbull.56.1.1.

Chalmers, G.R.L., Bustin, R.M., 2007. The organic matter distribution and methane capacity of the Lower Cretaceous strata of Northeastern British Columbia, Canada. Int. J. Coal Geol. 70, 223–239. https://doi.org/10.1016/j.coal.2006.05.001.

Cheng, A.L., Huang, W.L., 2004. Selective adsorption of hydrocarbon gases on clays and organic matter. Org. Geochem. 35 (4), 413–423. https://doi.org/10.1016/j.orggeochem.2004.01.007.

Cheng, P., Xiao, X.M., Tian, H., Gai, H.F., Zhou, Q., Li, T.F., Fan, Q.Z., 2022. Differences in the distribution and occurrence phases of pore water in various nanopores of marine-terrestrial transitional shales in the Yangquan area of the northeast Qinshui Basin, China. Mar. Petrol. Geol. 137, 105510. https://doi.org/10.1016/j.marpetgeo.2021.105510.

Feng, Y., Xiao, X.M., Gao, P., Wang, E.Z., Hu, D.F., Liu, R.B., Li, G., Lu, C.G., 2023a. Restoration of sedimentary environment and geochemical features of deep marine Longmaxi shale and its significance for shale gas: a case study of the Dingshan area in the Sichuan Basin, South China. Mar. Petrol. Geol. 151, 106186. https://doi.org/10.1016/j.marpetgeo.2023.106186.

Feng, Y., Xiao, X.M., Wang, E.Z., Gao, P., Lu, C.G., Li, G., 2023b. Gas storage in shale pore system: a review of the mechanism, control and assessment. Petrol. Sci. 20, 2605–2636. https://doi.org/10.1016/j.petsci.2023.05.012.

Fang, R.H., Liu, X.Q., Zhang, C., Li, M.J., Xia, X.H., Huang, Z.L., Yang, C.Y., Han, Q.Y., Tang, H.Q., 2022. Molecular simulation of shale gas adsorption under temperature and pressure coupling: case study of the Lower Cambrian in western Hubei Province. Nat. Gas Geosci. 33 (1), 138–152. https://doi.org/10.11764/j.issn.1672–1926.2021.07.017 (in Chinese).

Ge, M.N., Chen, K., Chen, X.L., Wang, C., Bao, S.J., 2020. The influence factors of gas-bearing and geological characteristics of Niutitang Formation shale in the southern margin of Xuefeng Mountain ancient uplift: a case of Well Huangdi 1. China Geology 3 (4), 533–544. https://doi.org/10.31035/cg2020072.

Guo, T.L., Zhang, H.R., 2014. Formation and enrichment mode of Jiaoshiba shale gas field, Sichuan Basin. Petrol. Explor. Dev. 41 (1), 28–36. https://doi.org/10.11698/PED.2014.01.03.

Gasparik, M., Bertier, P., Gensterblum, Y., Ghanizadeh, A., Krooss, B.M., Littke, R., 2014. Geological controls on the methane storage capacity in organic-rich shales. Int. J. Coal Geol. 123, 34–51. https://doi.org/10.1016/j.coal.2013.06.010.

Gasparik, M., Ghanizadeh, A., Bertier, P., Gensterblum, Y., Bouw, S., Krooss, B.M., 2012. High-pressure methane sorption isotherms of black shales from The Netherlands. Energy Fuel. 26, 4995–5004. https://doi.org/10.1021/ef300405g.

Hao, F., Zou, H., Lu, Y., 2013. Mechanisms of shale gas storage: implications for shale gas exploration in China. AAPG (Am. Assoc. Pet. Geol.) Bull. 97 (8), 1325–1346. https://doi.org/10.1306/02141312091.

Ji, L.M., Qiu, J.L., Zhang, T.W., Xia, Y.Q., 2012a. Experiments on methane adsorption of common clay minerals in shale. Earth Sci. J. China Univ. Geosci. 37 (5), 1043–1050. https://doi.org/10.3799/dqkx.2012.111 (in Chinese).

Ji, L.M., Zhang, T.W., Milliken, K.L., Qu, J.L., Zhang, X.L., 2012b. Experimental investigation of main controls to methane adsorption in clay-rich rocks. Appl. Geochem. 27 (12), 2533–2545. https://doi.org/10.1016/j.apgeochem.2012.08.027.

Liu, Z.B., Gao, B., Zhang, Y.Y., Du, W., Feng, D.J., Nie, H.K., 2017. Types and distribution of the shale sedimentary facies of the lower cambrian in upper Yangtze area, south China. Petrol. Explor. Dev. 44 (1), 21–31. https://doi.org/10.11698/PED.2017.01.03.

Li, G., Bai, G.P., Gao, P., Ma, S.H., Chen, J., Qiu, H.H., 2021. Geological characteristics and distribution of global primary hydrocarbon accumulations of Precambrian-Lower Cambrian. Petroleum Geology & Experiment 43 (6), 958–966. https://doi.org/10.11781/sysydz202106958 (in Chinese).

Lin, T., Zhang, J.C., Li, B., Yang, S.Y., He, W., Tang, X., Ma, L.R., Pei, S.W., 2014. Shale gas accumulation conditions and gas-bearing properties of the lower cambrian niutitang formation in well changye 1, northwestern hunan. Acta Pet. Sin. 35 (5), 839–846. https://doi.org/10.7623/syxb201405003 (in Chinese).

Li, G., Gao, P., Xiao, X.M., Lu, C.G., Feng, Y., 2022a. Lower Cambrian organic-rich shales in southern China: a review of gas-bearing property, pore structure, and their controlling factors. Geofluids, 9745313. https://doi.org/10.1155/2022/9745313, 2022.

Luo, S.Y., Chen, X.H., Li, H., Liu, A., Wang, C.S., 2019a. Shale gas accumulation conditions and target optimization of lower cambrian Shuijingtuo Formation in Yichang area, west Hubei. Earth Sci. 44 (11), 3598–3615. https://doi.org/10.3799/dqkx.2019.179 (in Chinese).

Luo, S.Y., Liu, A., Li, H., Chen, X.H., Zhang, M., 2019b. Gas-bearing characteristics and controls of the cambrian Shuijingtuo Formation in Yichang area, middle Yangtze region. Petroleum Geology and Experiment 41 (1), 56–67. https://doi.org/10.11781/sysydz201901056 (in Chinese).

Liu, Z.X., Yan, D.T., Yuan, D.E., Niu, X., Fu, H.J., 2022. Multiple controls on the organic matter accumulation in early Cambrian marine black shales, middle Yangtze Block, South China. Mar. Petrol. Geol. 100, 104454. https://doi.org/10.1016/j.jngse.2022.104454.

Liu, D.H., Xiao, X.M., Tian, H., Min, Y.S., Zhou, Q., Cheng, P., Shen, J.G., 2013. Sample maturation calculated using Raman spectroscopic parameters for solid organics: methodology and geological applications. Chin. Sci. Bull. 58 (11), 1285–1298. https://doi.org/10.1007/s11434–012–5535–y.

Li, G., Xiao, X.M., Gai, H.F., Feng, Y., Lu, C.G., Meng, G.M., 2022b. Nanopore structure evolution of Lower Cambrian shale in the western Hubei area, Southern China, and its geological implications based on thermal simulation experimental results. Nat. Resour. Res. 32 (2), 731–754. https://doi.org/10.1007/s11053–022–10149–1.

Li, G., Xiao, X.M., Gai, H.F., Lu, C.G., Feng, Y., 2023a. Nanopore structure characteristics and controlling mechanism of the Lower Cambrian shale reservoir in the western Hubei area, South China. J. Asian Earth Sci. 254, 105738. https://doi.org/10.1016/j.jseaes.2023.105738.

Li, G., Gao, P., Lu, C.G., Feng, Y., Meng, G.M., Li, D.S., Xiao, X.M., 2023b. Fractal Characteristics of Nanopores and Their Controlling Factors of the Lower Cambrian Shale in the Western Hubei Area, South China. Energy & Fuels. 37, 18801–18816. https://doi.org/10.1021/acs.energyfuels.3c02928.

Li, J., Zhou, S.X., Gaus, G., Li, Y.J., Ma, Y., Chen, K.F., Zhang, Y.H., 2018. Characterization of methane adsorption on shale and isolated kerogen from the Sichuan Basin under pressure up to 60 MPa: experimental results and geological implications. Int. J. Coal Geol. 189, 83–93. https://doi.org/10.1016/j.coal.2018.02.020.

Li, T.F., Tian, H., Xiao, X.M., Cheng, P., Zhou, Q., Wei, Q., 2017. Geochemical characterization and methane adsorption capacity of overmature organic-rich Lower Cambrian shales in northeast Guizhou region, Southwest China. Mar. Petrol. Geol. 86, 858–873. https://doi.org/10.1016/j.marpetgeo.2017.06.043.

Luo, S.Y., Chen, X.H., Yue, Y., Li, P.J., Cai, Q.S., Yang, R.Z., 2020. Analysis of sedimentary-tectonic evolution characteristics and shale gas enrichment in Yichang area, Middle Yangtze. Nat. Gas Geosci. 31 (8), 1052–1068. https://doi.org/10.11764/j.issn.1672–1926.2020.04.031 (in Chinese).

Li, H., Liu, A., Luo, S.Y., Chen, X.H., Chen, L., 2019. Characteristics of the cambrian Shuijingtuo shale reservoir on Yichang slope, western Hubei province: a case study of well EYY 1. Petroleum Geology and Experiment 41 (1), 76–82. https://doi.org/10.11781/sysydz201901076 (in Chinese).

Meng, G.M., Li, T.F., Gai, H.F., Xiao, X.M., 2022. Pore characteristics and gas preservation of the lower cambrian shale in a strongly deformed zone, northern chongqing, China. Energies 15, 2956. https://doi.org/10.3390/en15082956.

Ma, Y., Zhong, N.N., Li, D.H., Pan, Z.J., Cheng, L.J., Liu, K.Y., 2015. Organic matter/clay mineral intergranular pores in the Lower Cambrian Lujiaping Shale in the north-eastern part of the upper Yangtze area, China: a possible microscopic mechanism for gas preservation. Int. J. Coal Geol. 137, 38–54. https://doi.org/10.1016/j.coal.2014.11.001.

Murata, K., El-Merraoui, M., Kaneko, K., 2001. A new determination method of absolute adsorption isotherm of supercritical gases under high pressure with a special relevance to density-functional theory study. J. Chem. Phys. 114 (9), 4196–4205. https://doi.org/10.1063/1.1344926.

Murata, K., Miyawaki, J., Kaneko, K., 2002. A simple determination method of the absolute adsorbed amount for high pressure gas adsorption. Carbon 40, 425–428. https://doi.org/10.1016/s0008–6223(01)00126–9.

Pu, B.L., Dong, D.Z., Wang, F.Q., Wang, Y.M., Huang, J.L., 2020. The effect of sedimentary facies on Longmaxi shale gas in southern Sichuan Basin. Chin. Geol. 47

(1), 111–120. https://doi.org/10.12029/gc20200109 (in Chinese).
Pan, L., Xiao, X.M., Tian, H., Zhou, Q., Cheng, P., 2016. Geological models of gas in place of the longmaxi shale in southeast chongqing, south China. Mar. Petrol. Geol. 73, 433–444. https://doi.org/10.1016/j.marpetgeo.2016.03.018.
Rexer, T.F.T., Benham, M.J., Aplin, A.C., Thomas, K.M., 2013. Methane adsorption on shale under simulated geological temperature and pressure conditions. Energy Fuels 27, 3099–3106. https://doi.org/10.1021/ef400381v.
Rouquerol, J., Avnir, D., Fairbridge, C.W., Everett, D.H., Haynes, J.H., Pernicone, N., Ramsay, J.D.F., Sing, K.S.W., Unger, K.K., 1994. Physical chemistry division commission on colloid and surface chemistry, subcommittee on characterization of porous solids: recommendations for the characterization of porous solids. Pure Appl. Chem. 66 (8), 1739–1758.
Ross, D.J.K., Bustin, R.M., 2009. The importance of shale composition and pore structure upon gas storage potential of shale gas reservoirs. Mar. Petrol. Geol. 26, 916–927. https://doi.org/10.1016/j.marpetgeo.2008.06.004.
Rexer, T.F.T., Mathia, E.J., Aplin, A.C., Thomas, K.M., 2014. High-pressure methane adsorption and characterization of pores in Posidonia Shales and isolated kerogens. Energy Fuels 28 (5), 2886–2901. https://doi.org/10.1021/ef402466m.
Shi, S.F., 2020. Sedimentary Facies and the Law of Shale Gas Accumulation of Niutitang Formation of Lower Cambrian in Western Hubei. Chengdu University of Technology. https://doi.org/10.26986/d.cnki.gcdlc.2020.001139 (in Chinese).
Sun, J., Xiao, X.M., Cheng, P., 2021. Influence of water on shale pore heterogeneity and the implications for shale gas-bearing property - a case study of marine Longmaxi Formation shale in northern Guizhou. Mar. Petrol. Geol. 134, 105379. https://doi.org/10.1016/j.marpetgeo.2021.105379.
Sakurovs, R., Day, S., Weir, S., Duffy, G., 2007. Application of a modified Dubinin - radushkevich equation to adsorption of gases by coals under supercritical conditions. Energy Fuels 21, 992–997. https://doi.org/10.1021/ef0600614.
Sun, J., Xiao, X.M., Cheng, P., 2022. Methane absorption of coal-measure shales with and without pore water from the Qinshui Basin, North China: based on high-pressure methane absorption experiments. Int. J. Coal Geol. 263, 104116. https://doi.org/10.1016/j.coal.2022.104116.
Sircar, S., 1992. Estimation of isosteric heats of adsorption of single gas and multicomponent gas mixtures. Ind. Eng. Chem. Res. 31, 1813–1819. https://doi.org/10.1021/ie00007a030.
Tian, H., Pan, L., Zhang, T.W., Xiao, X.M., Meng, Z.P., Huang, B.J., 2015. Pore characterization of organic-rich lower cambrian shales in qiannan depression of guizhou province, southwestern China. Mar. Petrol. Geol. 62, 28–43. https://doi.org/10.1016/j.marpetgeo.2015.01.004.
Tian, H., Li, T.F., Zhang, T.W., Xiao, X.M., 2016. Characterization of methane adsorption on overmature Lower Silurian-Upper Ordovician shales in Sichuan Basin, southwest China: experimental results and geological implications. Int. J. Coal Geol. 156, 36–49. https://doi.org/10.1016/j.coal.2016.01.013.
Tang, X., Ripepi, N., Stadie, N.P., Yu, L., Hall, M.R., 2016. A dual-site Langmuir equation for accurate estimation of high pressure deep shale gas resources. Fuel 185, 10–17. https://doi.org/10.1016/j.fuel.2016.07.088.
Wei, G.Q., Yang, W., Xie, W.R., Jin, H., Su, N., Sun, A., Shen, Y.H., Hao, C.G., 2018. Accumulation modes and exploration domains of Sinian-Cambrian natural gas in Sichuan Basin. Acta Pet. Sin. 39 (12), 1317–1327. https://doi.org/10.7623/syxb201812001 (in Chinese).
Wang, K.M., 2021. Geological characteristics and controlling factors of shale gas accumulation of the Lower Cambrian in the southern Anhui of Lower Yangtze area. China Petroleum Exploration 26 (5), 83–99. https://doi.org/10.3969/j.issn.1672–7703.2021.05.008 (in Chinese).
Wang, M.L., Xiao, X.M., Wei, Q., Zhou, Q., 2015. Thermal maturation of solid bitumen in shale as revealed by Raman spectroscopy. Nat. Gas Geosci. 26 (9), 1712–1718. https://doi.org/10.11764/j.issn.1672–1926.2015.09.1712 (in Chinese).
Wang, P.F., Jiang, Z.X., Han, B., Lv, P., Jin, C., Zhang, K., Li, X., Li, T.W., 2018. Reservoir geological parameters for efficient exploration and development of Lower Cambrian Niutitang Formation shale gas in South China. Acta Pet. Sin. 39 (2), 152–162. https://doi.org/10.7623/syxb201802003 (in Chinese).
Wei, S.L., He, S., Pan, Z.J., Guo, X.W., Yang, R., Dong, T., Yang, W., Gao, J., 2019. Models of shale gas storage capacity during burial and uplift: application to Wufeng - longmaxi shales in the Fuling shale gas field. Mar. Petrol. Geol. 109, 233–244. https://doi.org/10.1016/j.marpetgeo.2019.06.012.
Wei, S.L., 2020. Reservoir Characteristics and Shale Gas Occurrence Mechanism of the Lower Cambrian Shuijingtuo Shale in the South of Huangling Anticline, Western Hubei. China University of Geosciences, Wuhan. https://doi.org/10.27492/d.cnki.gzdzu.2020.000081 (in Chinese).
Wang, Y.C., 2018. On shale organic geochemical characteristics of Niutitang Formation in western Hunan-Hubei area. Journal of Jianghan Petroleum University of Staff and Workers 31 (1), 8–10 (in Chinese).
Wu, J., Li, H., Goodarzi, F., 2022. Geochemistry and depositional environment of the Mesoproterozoic Xiamaling shales, northern North China. J. Pet. Sci. Eng. 215, 100730. https://doi.org/10.1016/j.petrol.2022.110730.
Wang, B.Q., Xiao, Y.X., Xu, Q.C., 2022. Structural evolution of the Huangling uplift, South China: implications for the shale gas exploration in the middle and lower Yangtze River area. J. Geomechanics 28 (4), 561–572. https://doi.org/10.12090/j.issn.1006–6616.2021130 (in Chinese).
Wang, S.J., Yang, T., Zhang, G.S., Li, D.H., Chen, X.M., 2012. Shale gas enrichment factors and the selection and evaluation of the core area. Strategic Study of CAE 14 (6), 94–100 (in Chinese).
Xiao, X.M., Wang, M.L., Wei, Q., Tian, H., Pan, L., Li, T.F., 2015. Evaluation of Lower Paleozoic shale with shale gas prospect in south China. Nat. Gas Geosci. 26 (8), 1433–1445. https://doi.org/10.11764/j.issn.1672–1926.2015.08.1433 (in Chinese).
Xu, L.L., Liu, Z.X., Wen, Y.R., Zhou, X.H., Luo, F., 2020. Shale gas reservoir and gas-bearing properties of middle Yangtze niutitang formation in western Hubei. Special Oil Gas Reservoirs 27 (4), 1–9. https://doi.org/10.3969/j.issn.1006–6535.2020.04.001 (in Chinese).
Xu, L.W., Yang, K.J., Wei, H., Liu, L.F., Jiang, Z.X., Li, Xiao, Chen, L., Xu, T., Wang, X.M., 2021. Pore evolution model and diagenetic evolution sequence of the Mesoproterozoic Xiamaling shale in Zhangjiakou, Hebei. J. Petrol. Sci. Eng. 207, 109115. https://doi.org/10.1016/j.petrol.2021.109115.
Zou, C.N., Dong, D.Z., Wang, S.J., Li, J.Z., Li, X.J., Wang, Y.M., Li, D.H., Cheng, K.M., 2010. Geological characteristics and resource potential of shale gas in China. Petrol. Explor. Dev. 37 (6), 641–653.
Zhang, J.F., Xu, H., Zhou, Z., Ren, P.F., Guo, J.Z., Wang, Q., 2019. Geological characteristics of shale gas reservoir in Yichang area, western Hubei. Acta Pet. Sin. 40 (8), 887–899. https://doi.org/10.7623/syxb201908001 (in Chinese).
Zhao, W.Z., Li, J.Z., Yang, T., Yang, T., Wang, S.F., Huang, J.L., 2016. Geological difference and its significance of marine shale gases in South China. Petrol. Explor. Dev. 43 (4), 499–510. https://doi.org/10.11698/PED.2016.04.01.
Zhai, G.Y., Bao, S.J., Wang, Y.F., Chen, K., Wang, S.J., Zhou, Z., Song, T., Li, H.H., 2017a. Reservoir accumulation model at the edge of palaeohigh and significant discovery of shale gas in Yichang area, Hubei Province. Acta Geosci. Sin. 38 (4), 441–447. https://doi.org/10.3975/cagsb.2017.04.01 (in Chinese).
Zhai, G.Y., Wang, Y.F., Liu, G.H., Lu, Y.C., He, S., Zhou, Z., Li, J., Zhang, Y.X., 2020. Accumulation model of the Sinian-Cambrian shale gas in western Hubei Province, China. J. Geomechanics 26 (5), 696–713. https://doi.org/10.12090/j.issn.1006–6616.2020.26.05.058 (in Chinese).
Zhai, G.Y., Wang, Y.F., Bao, S.J., Guo, X.T., Zhou, Z., Chen, X.L., Wang, J.Z., 2017b. Major factors controlling the accumulation and high productivity of marine shale gas and prospect forecast in Southern China. Earth Sci. 42 (7), 1057–1068. https://doi.org/10.3799/dqkx.2017.085 (in Chinese).
Zhai, G.Y., Li, J., Jiao, Y., Wang, Y.F., Liu, G.H., Xua, Q., Wang, C., Chen, R., Guo, X.B., 2019. Applications of chemostratigraphy in a characterization of shale gas Sedimentary Microfacies and predictions of sweet spots-taking the Cambrian black shales in Western Hubei as an example. Mar. Petrol. Geol. 109, 547–560. https://doi.org/10.1016/j.marpetgeo.2019.06.045.
Zuo, J.X., Peng, S.C., Qi, Y.P., Zhu, X.J., Bagnoli, G., Fang, H.B., 2018. Carbon-isotope excursions recorded in the Cambrian System, South China: implications for mass extinctions and sea-level fluctuations. J. Earth Sci. 29 (3), 479–491. https://doi.org/10.1007/s12583–017–0963–x.
Zhou, Q., Xiao, X.M., Pan, L., Tian, H., 2014. The relationship between micro-Raman spectral parameters and reflectance of solid bitumen. Int. J. Coal Geol. 121, 19–25. https://doi.org/10.1016/j.coal.2013.10.013.
Zhang, T.W., Ellis, G.E., Ruppel, S.C., Milliken, K.L., Yang, R., 2012. Effect of organic matter type and thermal maturity on methane adsorption in shale-gas systems. Org. Geochem. 47, 120–131. https://doi.org/10.1016/j.orggeochem.2012.03.012.
Zhou, L., Zhou, Y., Li, M., Chen, P., Wang, Y., 2000. Experimental and modeling study of the adsorption of supercritical methane on a high surface activated carbon. Langmuir 16, 5955–5959. https://doi.org/10.1021/la991159w.
Zhou, W., Xu, H., Yu, Q., Xie, R.C., Deng, K., 2016. Shale gas-bearing property differences and their genesis between Wufeng-Longmaxi Formation and Qiongzhusi Formation in Sichuan Basin and surrounding areas. Lithologic Reservoirs 28 (5), 18–25. https://doi.org/10.3969/j.issn.1673–8926.2016.05.002 (in Chinese).
Zhang, T.W., Luo, H., Meng, K., 2023. Main factors controlling the shale gas content of Cambrian shales of southern China - a discussion. Earth Sci. Front. 30 (3), 1–13. https://doi.org/10.13745/j.esf.sf.2022.5.31 (in Chinese).